1 **Dynamic fault interaction during a fluid-injection induced earthquake: The**

2 **2017 Mw 5.5 Pohang event**

3 - **Kadek Hendrawan Palgunadi[1]** : **kadek.palgunadi@kaust.edu.sa**

4 - **Alice-Agnes Gabriel[2]** : **gabriel@geophysik.uni-muenchen.de**

5 - **Thomas Ulrich[2]** : **ulrich@geophysik.uni-muenchen.de**

6 - **José Ángel Lopéz-Comino[3i]** : **lopezcomino@uni-potsdam.de**

7 - **Paul Martin Mai[1]** : **martin.mai@kaust.edu.sa**

8

9 1. Physical Science and Engineering, King Abdullah University of Science and Technology, Thuwal, Saudi Arabia

10 2. Department of Earth and Environmental Sciences, Geophysics, Ludwig-Maximilians-Universität München,

11 Theresienstr. 41, 80333 Munich, Germany

12 3. Institute of Geosciences University of Potsdam, Potsdam-Golm, Germany.

13

[i]also at Instituto Andaluz de Geofísica, Universidad de Granada, Spain; Departamento de Física Teórica y del Cosmos, Universidad de Granada, Spain; Physical Science and Engineering, King Abdullah University of Science and Technology, Thuwal, Saudi Arabia

14 **Abstract**:

15 The November 15th, 2017 Mw 5.5 Pohang earthquake (South Korea) has been linked to hydraulic

16 stimulation and fluid injections, making this the largest induced seismic event associated with an

17 Enhanced Geothermal System (EGS). To understand its source dynamics and fault interactions,

18 we conduct the first 3D high-resolution spontaneous dynamic rupture simulations of an induced

19 earthquake. We account for topography, off-fault plastic deformation under depth-dependent bulk

20 cohesion, rapid velocity weakening friction and 1D subsurface structure. A guided fault

21 reconstruction approach that clusters spatio-temporal aftershock locations (including their

22 uncertainties) is used to identify a main and a secondary fault plane which intersect under a shallow

23 angle of 15°. Based on simple Mohr-Coulomb failure analysis and 180 dynamic rupture

24 experiments in which we vary local stress loading conditions, fluid pressure, and relative fault

25 strength, we identify preferred two fault plane scenarios that well reproduce observations. We find

26 that the regional far-field tectonic stress regime promotes pure strike-slip faulting, while local

27 stress conditions constrained by borehole logging generate the observed thrust faulting component.

28 Our preferred model is characterized by overpressurized pore fluids, non-optimally oriented but

29 dynamically weak faults and a close to critical local stress state. In our model, earthquake rupture

30 "jumps" to the secondary fault by dynamic triggering, generating a measurable non-double couple

31 component. Our simulations suggest that complex dynamic fault interaction may occur during

32 fluid-injection induced earthquakes and that local stress perturbations dominate over the regional

33 stress conditions. These findings, therefore, have important implications for seismic hazard in

34 active geo-reservoir.

35

36

Introduction

37

38   The Korean Peninsula is known to have a rather low-level of seismicity (compared to

39   neighboring countries like China and Japan) because it lies on the continental margin of the east

40   Eurasian plate. However, on November 15th, 2017 (05:29:31 UTC), a magnitude Mw 5.5

41   earthquake occurred (hereinafter the Pohang earthquake), the second-largest recorded earthquake

42   in South Korea following the 2016 M_L 5.8 Gyeongju earthquake. The Pohang earthquake caused

43   one fatality, injured 82 people, and generated more than \$300 millions in total economic loss

44   (Ellsworth et al., 2019; Lee et al., 2019). The hypocenter was located approximately 10 km

45   northeast of Pohang city, close to the Pohang Enhanced Geothermal System (EGS) site (36.106°N,

46   129.373°E and depth ~4.27 km, Korean Government Commission, 2019). Its proximity to the EGS

47   site and hypocentral depth similar to the open hole sections of the fluid-injection wells (Figure 1)

48   quickly raised questions if this earthquake is associated with EGS activities (Grigoli et al., 2018;

49   Kim et al., 2018).

50   The Pohang EGS project was designed to create an enhanced geothermal reservoir within

51   a low permeability crystalline basement. The basement is overlain by cretaceous volcanic and

52   sedimentary rocks, tertiary volcanic and sedimentary rocks, and quaternary sediments (Korean

53   Government Commission, 2019; Ellsworth et al., 2019). During a period of four years (2012 to

54   2016), two geothermal wells (maximum depth ~4.3 km) were drilled for hydraulic stimulations.

55   At the surface, both wells are separated by only 6 m distance, increasing to a separation of 599 m

56   at a depth of ~4.3 km. For well PX-1, the drilling was stuck at a depth of 2419 m, and hence side-

57   tracked into west-northwest direction. Well PX-2 experienced large mud loss in the depth interval

58   3830 - 3840 m, while cuttings contain significant fractions of friable round-shaped mud balls

59   typical for fault gouge (Korean Government Commission, 2019; Ellsworth et al., 2019). In these

60 geothermal wells, five hydraulic stimulations were conducted between 29 January 2016 and 18

61 September 2018. During this period, each hydraulic stimulation phase was associated with

62 seismicity. The magnitudes during and after stimulations reached up to $M_L \approx 3$, while events were

63 distributed within a restricted area close to the wells (Woo et al., 2019). The depth of the seismicity

64 before the Pohang earthquake spans the depth range 3.8 to 4.4 km, comparable with the open-hole

65 section of the well at ~4.3 km depth (Ellsworth et al., 2019).

66 Recent studies confirm that the Pohang earthquake was induced by hydraulic stimulation

67 and extensive fluid injection at this EGS site (Korean Government Commission, 2019; Ellsworth

68 et al., 2019; Woo et al., 2019; Kim et al., 2020). These activities are considered to have activated

69 the previously unmapped fault which was found to intersect well PX-2 at a depth of ~3.8 km.

70 Chang et al. (2020) point out that increased pore-pressure stressing due to multiple injection wells

71 at the Pohang EGS site may have contributed to the mainshock generation. However, it has been

72 argued that the size of fluid-injection induced earthquakes can be controlled by managing pressure,

73 location, and rate of fluid injection (Hofmann et al., 2019). Data-driven empirical and numerical

74 studies have shown that the induced earthquakes are confined by a function of injected volume

75 (McGarr, 2014; Galis et al., 2017).

76 Grigoli et al. (2018) find a complex-source mechanism for the Pohang earthquake with a

77 significant non-double couple (non-DC) component. They hypothesized that this earthquake

78 involved failure on two different faults with slightly different focal mechanisms. In fact, in EGS

79 reservoirs with extensive fluid injection and hydraulic stimulation, earthquakes with pronounced

80 non-DC components may occur (Julian et al., 1998). Moreover, fluid injections may induce local

81 deviation of the stress state from the regional stress regime (Schoenball et al., 2014; Martínez-

82 Garzón et al., 2013; Martínez-Garzón et al., 2014). Therefore, we examine how regional and local

83   stress conditions acting on different fault models (single plane and two planes) determine the

84   dynamic rupture process that leads to a source mechanism with non-DC components.

85   Dynamic rupture modeling aims to reproduce the physical processes that govern how

86   earthquakes start, propagate, and stop for given stress and frictional conditions acting on fault

87   surfaces. The earthquake dynamics are then a result of the model's initial conditions, such as

88   geometry and frictional strength of the fault(s), the tectonic stress state, the regional lithological

89   structure, and a frictional constitutive equation. Jin and Zoback (2018) model coseismic fully

90   dynamic spontaneous fault rupture resulting from preseismic quasi-static loading exerted by fluid

91   perturbations in a faulted porous medium in 2D. Duan (2016) model 2D dynamic rupture

92   accounting for fluid effects of a propagating hydraulic fracture. Cappa and Ruitquist (2012) and

93   Buijze et al. (2017) constrain the onset of 2D dynamic rupture experiments by the stress state

94   resulting from solving a coupled quasi-static poroelastic equation. Further 2D studies that model

95   induced (not fully dynamic) earthquake rupture linked to separately treated fluid diffusion

96   including Galis et al. (2017); Kroll et al., (2017); Dieterich et al. (2015); Garagash and

97   Germanovich (2012); Richards-Dinger and Dieterich (2012); Viesca and Rice (2012). Using

98   modern numerical methods and advanced hardware, a high degree of realism can be reached to

99   explicitly model in 3D the highly non-linear dynamic rupture process (e.g., Heinecke et al., 2014;

100   Roten et al., 2014; Uphoff et al., 2017; Wollherr et al., 2019; Ulrich et al., 2019a, 2019b). The

101   modeling results include spatial and temporal evolution of earthquake rupture, surface

102   displacements, and ground shaking caused by the radiated seismic waves.

103   In this study, we investigate the dynamic rupture process under variable stress and fault-

104   geometry assumptions for the Pohang earthquake, using the high-performance-computing (HPC)

105   enabled software package SeisSol (see **Data and Resources**). Two alternative fault geometries are

106   considered, a one fault plane model (Model 1F) and a two fault planes model (Model 2F). In our

107   simulations, we consider a 1D velocity structure (Woo et al., 2019), off-fault plasticity (Wollherr

108   et al., 2018), depth-dependent bulk cohesion, a rapid velocity weakening friction law, borehole

109   estimates of stress, complex fault geometry, and high-resolution topography.

110   In the following, we first describe (Section 2) a new observationally guided fault

111   reconstruction approach based on spatio-temporal clusters of microearthquakes and their spatial

112   uncertainty. In Section 3, we analyse initial fault strength and loading stresses using static and

113   dynamic rupture modeling. We then compare the dynamics and kinematics of two preferred

114   models, Model 1F and 2F. The validation of Model 2F with regional waveforms, as well as

115   comparison of surface deformation between Model 1F and Model 2F are also presented in Section

116   3. Finally, we discuss the importance of considering local stresses loading, apparently weak and

117   critically stressed faults, overpressurized fluids, and dynamic multiple fault interaction in EGS.

118

Modeling Setup

119

120   In the following, we describe our approach to produce a physically viable model

121   constrained by observational data. Dynamic rupture propagation is governed by fault strength,

122   fault geometry, subsurface material properties, topography, loading ("initial") stresses, nucleation

123   procedure, and empirical friction laws (Dunham et al., 2011a; Harris et al., 2011; Harris et al.,

124   2018). Numerical experiments that vary the aforementioned parameters provide insights into

125   fundamental earthquake physics as well as serve to identify preferred, self-consistent scenarios

126   that explain the mechanical processes of the earthquake as well as observational data.

127

128   **Fault reconstruction**

129   The detailed fault geometry has a strong effect on the dynamic rupture process. Changes

130   in strike, dip, and deviations from fault planarity can impact the rupture propagation and the

131   corresponding physical processes. The Pohang earthquake occurred on one or several blind and

132   unmapped fault(s). Because the unwrapped InSAR surface-displacement data show unclear fringes

133   due to the small deformation around the epicenter (Choi et al., 2019; Song and Lee, 2019), we use

134   the high-resolution earthquake catalog from Kim et al. (2018) to constrain the fault geometry based

135   on a space-time (including their uncertainties in space) clustering approach. The earthquake

136   catalog spans from 9 hours before to 3 hours after the mainshock and contains 217 events.

137

138   **Spatio-temporal clustering**

139   Clustering techniques allow deciphering complex fault structures by associating seismic

140   events to groups (clusters), also discriminating events that are associated with the mainshock from

141   uncorrelated earthquakes. We examine the seismic sequence to separate seismic clusters and

142   background events using nearest-neighbor distances following Zaliapin and Ben-Zion (2013). The

143   dependence of an event i to a parent event j is determined from the nearest-neighbor distance η_{ij}:

144

145    $$\eta_{ij} = dt_{ij} \times dr_{ij}{}^{d} \, , d_{ij} > 0; \ \eta_{ij} = \infty, dt_{ij} < 0 \qquad\qquad (1)$$

146

147   where $dt_{ij} = t_j - t_i$ is the time between event i and j, $dr_{ij} = (r_j - r_i)$ is the interevent distance

148   between events; r_i = coordinate of event i and r_j = coordinate of event j, and d is the fractal

149   dimension of the earthquake hypocenter distribution (Hirata, 1989). We find that the inferred

150   clusters are not very sensitive to the parameter d; hence we set $d = 1.6$ following previous studies

151   (Zaliapin and Ben-Zion, 2013; Zhang and Shearer, 2016; Cheng and Chen, 2018). Based on this

152   analysis, we find that all earthquakes of the catalog are part of the cluster and can be used for fault-

153   plane fitting (see Figure 2a). This cluster is characterized by interevent distances less than 1 km.

154

Fault plane fitting

156   We adopt the anisotropic clustering location uncertainty distribution (ACLUD) method, a

157   fault-network reconstruction approach introduced by Wang et al. (2013), which accounts for

158   uncertainties in earthquake locations. This method is extended by considering regional tectonic

159   constraints, focal mechanisms, and surface geological manifestation as prior information, leading

160   to the following improvements in the original ACLUD algorithm:

161   1) Initialize N_0 number of faults following the predefined orientation of the S_{Hmax} extracted

162   from the world stress map with random position and size.

163   2) For each cluster, if more than four similar focal mechanisms (strike, dip, rake) are available,

164   we use this information to separate events that have distinct focal mechanisms into other

165   clusters.

166   3) If surface geological manifestation (fault traces) exists (not the case for this study), the

167   strike and dip of the generated fault segment(s) should follow the closest interpreted fault

168   trace orientation.

169   We refer to this modified ACLUD method as guided-ACLUD (g-ACLUD).

170   All explored solutions are subject to a statistical validation process that examines the

171   likelihood of each proposed fault-network, given all available focal mechanisms. Statistical

172   validation uses the Bayesian Information Criterion (BIC). Initially, the method uses a random

173   number of fault planes. A single fault plane may be split if the BIC remains high. On the other

174   hand, two close-enough fault planes with similar orientation (strike and dip) may be merged into

175   a single fault plane. The process is repeated until the BIC reaches a pre-defined minimum or if the

176   process exceeds the maximum specified number of iterations (Wang et al., 2013).

177   The ACLUD algorithm by Wang et al. (2013) uses event locations and the associated

178   uncertainties given by the earthquake catalog. We incorporate additional information to increase

179   the robustness of the results and to decrease the explored parameter space. As *a priori* information,

180   we use the orientation of the maximum compressive regional stress given by the world stress map

181   (Heidbach et al. 2018) and available focal mechanisms in the area which are associated with the

182   earthquake catalog. Therefore, we use a maximum horizontal stress orientation of 74° with an

183   uncertainty of 25° and consider the focal mechanism inferred by Grigoli et al. (2018). Since

184   location errors are not specified in this earthquake catalog, we assume normally distributed

185   uncertainty for all events (standard deviation of 100 m). Note that Kim et al. (2018) obtained a

186   median error of 42, 31, and 36 m in the EW, NS, and vertical directions, respectively, but no

187   uncertainties for individual events.

188   Figure 2b, 2c, 2d show the g-ACLUD selected solution, characterized by the smallest BIC,

189   which features two intersecting planar fault planes. The main plane strikes at 214° and dips at 65°,

190   while the secondary fault plane strikes at 199° and dips 60°, respectively. The two fault planes are

191   separated by a narrow angle of 15°. The secondary fault aligns with the subsidiary fault plane

192   identified by Kim et al. (2018). The dimensions of the main and secondary fault planes are 4.3 km

193   x 2.8 km and 3.0 km x 2.2 km, respectively. As the goal of this study is to compare the rupture

194   process for two different fault configurations, we define a one fault plane geometry (Model 1F)

195   and a two fault planes geometry (Model 2F; derived fault reconstruction analysis). The single-fault

196   model has a fault plane striking 214° and dipping 43°, as suggested by Korean Government

197   Commission (2019), Ellsworth et al. (2019), and Woo et al. (2019).

198

Material properties

200 We assume an elasto-plastic, isotropic medium based on the 1D velocity profile (Figure

201 S1a; Woo et al. (2019)). The velocity profile honors geological structures observed from drilling

202 cores and seismological observations from both active and passive sources, for instance, vertical

203 seismic profiling (VSP) and well logging (Korean Government Commission, 2019; Woo et al.,

204 2019). The density distribution (Figure S1a) is adopted from the report by Korean Government

205 Commission (2019).

206 We use a computationally efficient implementation of a Drucker-Prager off-fault

207 viscoplastic rheology (Wollherr et al., 2018). The off-fault failure criterion is based on the internal

208 friction coefficient (bulk friction) and bulk cohesion. We assume a constant internal friction

209 coefficient equal to the prescribed on-fault friction coefficient ($\mu_{bulk-friction} = 0.6$) for the entire

210 model domain. However, bulk cohesion is set to be depth-dependent, accounting for geologic

211 strata in the Pohang EGS site and the hardening of rocks with depth. Therefore, bulk cohesion

212 ranges from $c = 4$ MPa near the surface to $c = 50$ MPa at a depth of 6 km. A lower bulk cohesion

213 (12.5% of the surroundings) is applied in a 1.5 x 0.3 x 4 km^3 volume around the fault intersection

214 for the case of two fault planes to mimic pre-existing damage which enhances off-fault yielding

215 and to prevent unrealistic high on-fault stresses at the fault intersection. We assume initially

216 equivalent stresses acting on and off the fault. Finally, we set a constant, mesh-independent

217 relaxation time following the analysis by Wollherr et al., (2018) and chose $T_V = 0.05$ s, consistently

218 with choices made in previous studies (e.g. Ulrich et al., 2019a, 2019b).

219

Fault strength and loading stresses

221 To constrain the most viable principal stress component azimuth and the overall stress

222 regime, we extract information (e.g., S_{Hmax} orientation and fault strength) from laboratory and

223 field observation to then perform numerical experiments. We adopt a friction law with rapid

224 velocity weakening (adapted from Dunham et al., 2011a; see Appendix, **Friction parameters**)

225 which reproduces the rapid friction decrease observed in laboratory experiments at co-seismic slip

226 rates (Di Toro et al., 2011).

227 We parametrize fault friction aiming for realistic levels of static and dynamic frictional

228 resistance and stress drop. All frictional properties are detailed in Appendix (**Friction**

229 **parameters**). We apply velocity weakening ($b - a = 0.004$) across the fault (see Figure S1b) and

230 velocity strengthening ($b - a = -0.004$) to the uppermost part of the fault, which allows for a

231 smoother termination of the rupture there. The state evolution distance (L), initial slip rate (V_{ini}),

232 reference slip velocity (V_0), steady-state friction coefficient (f_0), and weakened friction coefficient

233 (f_w) are constant and depth-independent.

234 We follow the systematic approach of Ulrich et al. (2019a) to examine initial fault stress

235 and relative apparent fault strength combining data from observations, (e.g., seismo-tectonic

236 observations and fault fluid pressurization) and the Mohr-Coulomb theory of failure. This

237 workflow reduces the non-uniqueness in dynamic rupture modeling parameterization by assessing

238 that the stress state is compatible with the fault geometry and the fault-slip orientation (rake angle)

239 inferred from finite source or moment tensor inversion. Assuming an Andersonian stress regime

240 (one principal stress axis is vertical), only four parameters are sufficient to fully describe the stress

241 state and strength of the fault system: the azimuth of maximum compressive stress (S_{Hmax}), the

242 initial relative fault prestress ratio (R_0), the stress shape ratio (v), and the fluid pressure ratio (γ),

243 all detailed hereafter.

244   The Pohang EGS site is considered to be located within a strike-slip stress regime (Soh et

245   al., 2018, and references therein). This translates into the maximum principal stress being

246   horizontal ($s_1 = S_{Hmax}$, with principal stress components $s_1 > s_2 > s_3 > 0$) under Andersonian

247   stress. Previous studies examined the azimuth of maximum horizontal stress using different

248   methods, such as borehole and seismological techniques, e.g., stress inversion of focal mechanisms

249   (Kim et al., 2017; Lee et al., 2017; Lee, Hong, and Chang, 2017; Soh et al., 2018; Korean

250   Government Commission, 2019; Ellsworth et al., 2019). Soh et al. (2018) inferred S_{Hmax} from

251   focal mechanisms of earthquakes that occurred between 1997 and 2016 and determined a regional

252    $S_{Hmax} = 74°$. However, the earthquakes closest (~40 km) to the Pohang EGS site used in their

253   analysis are the 2016 Gyeongju event and its aftershocks. Based on borehole data, Kim et al. (2017)

254   and Lee, Shinn, et al. (2017) determined that S_{Hmax} at shallow depths (700 m to 1000 m) within a

255   10 km radius from the Pohang EGS is about 130°. In contrast, Ellsworth et al. (2019) and Korean

256   Government Commission (2019) inferred a critically stressed thrust faulting regime. This stress

257   state implies that the vertical stress is the least principal stress under Andersonian stress ($s_v = s_3$).

258   They inferred an S_{Hmax} orientation of $77 \pm 23°$ based on dipole sonic logging data. This

259   orientation is similar to the value of 74° given in the world stress map (Heidbach et al., 2018).

260   Using numerical simulations, we then assess how these loading-stress regimes for the

261   inferred fault geometry determine nucleation and rupture of the Pohang earthquake. The stress

262   shape ratio v enables a contrast of different stress styles by balancing the principal stress

263   amplitudes. It is defined as:

264

265           $v = \dfrac{(s_2 - s_3)}{(s_1 - s_3)}$ (2)

266

267   For strike-slip regimes (s_2 vertical), $v < 0.5$ characterizes transpression, $v \approx 0.5$ corresponds to

268   pure strike-slip regime, and $v > 0.5$ characterizes transtension (Ulrich et al., 2019a). Soh et al.

269   (2018) ($v = 0.12$), Ellsworth et al., (2019) and Korean Government Commission (2019) ($v = 0.1$)

270   suggests a stress regime acknowledging transpression around the Pohang EGS site (note that they

271   use different definition of v).

272   The initial relative prestress ratio (R_0) describes the closeness to failure on a virtual,

273   optimally oriented fault. $R_0 = 1$ indicates a critical stress level on all optimally oriented faults. We

274   can characterize fault strength spatially by calculating the relative prestress ratio (R) on every point

275   of the fault. R denotes the ratio of potential stress drop $\Delta\tau$ with respect to breakdown strength drop

276     $\Delta\tau_b$ for given frictional cohesion (c), static (μ_s) and dynamic (μ_d) friction coefficient (e.g., Aochi

277   and Madariaga, 2003) expressed as:

278

279         $R = \frac{\Delta\tau}{\Delta\tau_b} = \frac{\tau_0 - \mu_d\sigma_n}{c + (\mu_s - \mu_d)\times\sigma_n}$ (3)

280

281   where τ_0 and σ_n are initial shear and normal traction on the fault plane, respectively. However, in

282   this study, we neglect the contribution of frictional cohesion ($c = 0$), which is mostly important to

283   incorporate close to the Earth's surface. We assume $\mu_s = f_0 = 0.6$ and $\mu_d = f_w = 0.1$. The

284   relative prestress ratio can be related to the relative fault strength parameter (S) defined as $S =$

285     $1/R - 1$. On-fault values of R change at every point as we vary R_0, taking on values $R \leq R_0$

286   depending on the orientation of each fault point with respect to the optimal orientation.

287   The vertical principal stress is assumed to vary linearly with depth, consistent with the

288   geological strata (depth-dependent density (ρ) in Figure S1a). We assume the intermediate

289 principal stress component, s_2, to be vertical. The confining pressure of the overlying rock is

290 reduced by the pore pressure (P_f). We assume P_f proportional to lithostatic stress as $P_f = \gamma \rho g z$,

291 where g is the gravitational acceleration (9.8 m/s^2), and z denotes depth (in meters) and γ is the

292 fluid pressure ratio. A fluid pressure ratio of 0.37 indicates hydrostatic pore pressure, while $\gamma >$

293 0.37 implies an overpressurized stress state.

294   We perform a range of static and dynamic numerical experiments described below to test

295 the sensitivity of the resulting dynamic rupture models to the chosen stress parameterization in

296 terms of S_{Hmax}, R_0 and γ. We keep the 4th parameter, the stress shape ratio, fixed at $\nu = 0.12$

297 (Soh et al., 2018). We do not adjust the stress states for the stress excess during nucleation (see

298 Appendix, **Nucleation procedure**). The overstressed nucleation and its parameters are constant

299 for all 180 numerical experiments.

300

Results

302   We use the open-source software SeisSol (details in Appendix, **numerical method**) to

303 solve the elastodynamic equations of motion for fault rupture under stress and friction acting on

304 the fault surface, coupled to seismic wave propagation in complex media. We set the on-fault mesh

305 size using estimates of cohesive zone width (details in Appendix, **mesh generation**). We

306 incorporate high-resolution topography into our modeling. Figure 3 shows the computational mesh

307 overlain by a snapshot of absolute velocity at t = 5 s.

308   Next, we present 3D dynamic rupture simulations for scenarios that consider one and two

309 intersecting fault planes, incorporating depth-dependent regional loading stresses, off-fault plastic

310 yielding, and high-resolution surface topography. In the preferred model (Model 2F), the

311 secondary fault plane is dynamically triggered and can explain the observed non-double couple

312   component of the moment tensor solution. Our model is compatible with regional waveforms and

313   surface deformation derived from published InSAR analysis.

314

Static and dynamic analysis of initial fault strength and stresses

316   We first constrain the regional stress from purely static analysis. Figure S2 shows a few

317   cases (out of many permutations (see also Table S1)) we analyzed. The six examples shown use

318   parameters $\gamma = 0.5$ and $R_0 = 0.7$, and variable S_{Hmax} in the range 52° - 140°. According to the

319   static analysis, $S_{Hmax} < 87°$ is insufficient to generate a rake angle of shear traction compatible

320   with the thrust-faulting component inferred by the focal mechanism and moment tensor solution.

321   At $S_{Hmax} \geq 87°$, a thrust-faulting component starts to emerge. Interestingly, only the secondary

322   fault plane features a rake angle larger than 40° for $S_{Hmax} = 77° - 140°$. A rake angle of $\sim 80°$,

323   obtained with $S_{Hmax} = 120°$, can potentially produce the thrust-faulting component inferred by

324   moment tensor solution. For this parametrization, the secondary fault plane reaches a higher rake

325   angle of approximately 110°.

326   We restrict the parameter space for R_0 and γ based on our static analysis. We then

327   systematically explore all permutations of the three different parameters within the selected range

328   using dynamic rupture simulations. We vary R_0 in the range 0.7 - 0.9, γ within 0.37 - 0.9 and

329   S_{Hmax} within 67 - 120°. Figure 4 summarizes the outcome of 180 numerical dynamic rupture

330   experiments. We find that under hydrostatic pressure ($\gamma = 0.37$), $S_{Hmax} = 120°$ generates self-

331   sustained ruptures over any other S_{Hmax} orientation.

332   The thrust-faulting component generated with $S_{Hmax} = 67° - 87°$ is insufficient to

333   explain the seismological observation using dynamic rupture modeling. Such S_{Hmax} leads to pure

334   strike-slip faulting as the only mechanical viable solution. Both dynamic and static analyses

335   suggest that $S_{Hmax} = 120°$ is necessary to generate a thrust-faulting component close to the

336   observations. Our analyses allow determining a preferred parameterization, compatible with

337   inferred ground deformation, observed regional waveforms, and the inferred focal mechanism:

338     $R_0 = 0.8$ and $\gamma = 0.5$.

339

340   **Rupture dynamics of the preferred scenario Model 1F and Model 2F**

341   Figure 5a and Video S1 (in supplementary material) provide an overview of the simulated

342   earthquake rupture of the preferred two fault model Model 2F: rupture propagates spontaneously

343   across the main fault plane and dynamically triggers the secondary fault plane (rupture jumping).

344   The rupture nucleates smoothly due to the prescribed time-dependent overstress (see

345   Appendix, **Nucleation procedure**) centered at the hypocenter location; it then spontaneously

346   propagates bilaterally across the main fault plane. At a rupture time of 0.65 s, two successive slip-

347   rate fronts emerge, with lower peak slip rates than the main rupture front (Figure 5a, left). This

348   rupture complexity is associated with the simultaneous rupture on both fault planes, leading to

349   multiple reflected and trapped waves in-between the two fault planes, reactivating the main fault

350   around the intersection. Rupture complexity decreases as rupture on the secondary fault plane

351   terminates. After rupture time t = 0.75 s, we observe solely pulse-like rupture propagation across

352   the main fault.

353   The secondary fault plane is dynamically triggered at 0.4 s and its rupture terminates at 0.8

354   s simulation time, while the main-fault is fully ruptured in about 1.1 s. The secondary fault plane

355   is only partially ruptured because the northern part of the main fault does not slip. High slip-rates

356   (~ 10 m/s) and multiple rupture fronts occur near the fault intersection at the secondary fault.

357   Rupture heals close to the fault intersection region around $t = 0.65\ s$.

358   After $t = 0.75\ s$ rupture on the main fault dynamically clamps (e.g., Kyriakopoulos et al.,

359   2019) and thus does not facilitate direct branching to the northern unbroken part of the secondary

360   fault plane. We observe asymmetric peak slip-rate distribution (see Figure S3), with higher values

361   on the single fault plane part of the network (Figure 5a, right) and lower peak slip rates where

362   ruptures across directly adjacent fault planes interact, which is also associated with high off-fault

363   plastic yielding (see section **Off-fault deformation** below). The entire rupture is completed after

364   ~1.5 s simulation time, breaking 4 km of fault length and generating a moment magnitude of M_w

365   5.59 (dominated by slip on the main fault plane). We find that rupture stops smoothly and

366   spontaneously on the secondary fault plane and north-eastern part of the main fault plane, while

367   being stopped abruptly by the southwestern fault end of main fault plane.

368   In contrast to the Model 2F, the one fault plane preferred Model 1F produces symmetric

369   bilateral slip-rate and slip distributions.

370

Rupture kinematics of the preferred Model 1F and Model 2F scenarios

372   Due to the size of the event and limited available data, the kinematics of the Pohang

373   earthquake are challenging to characterize and explain. We here describe the model kinematics of

374   the preferred Model 1F and Model 2F earthquake scenarios. and compare both with two

375   observational studies (Song and Lee, 2019; Grigoli et al., 2018).

376   Song and Lee (2019) estimated the static slip distribution by InSAR (both descending and

377   ascending-descending orbit) for a single fault plane with patch size 0.5 by 0.5 km. Higher slip

378   predominantly occurs northeast of the hypocenter, with an average slip of 0.15 m (Song and Lee,

379   2019). Grigoli et al. (2018) applied an Empirical Green's Function (EGF) technique to study

380   rupture duration and directivity, suggesting an apparent rupture duration of ~1 s and ~3 s for

381   stations observed in the SE and NW direction, respectively. Their focal mechanism shows an

382   average rake of ~135°.

383   Both preferred scenarios vary slightly in moment magnitude, M_W 5.63 and M_W 5.59 for

384   Model 1F and Model 2F, reflecting different fault geometries while otherwise using the same

385   dynamic rupture model parametrization. We point out that most slip of Model 2F occurs on the

386   main fault - its magnitude is reduced to M_W 5.51 when removing the subsidiary plane.

387   The resulting synthetic source time functions of Model 1F and Model 2F are presented in

388   Figure 6a and 6b, respectively. The boxcar shaped moment rate function of Model 1F results from

389   its comparably simple rupture dynamics across one planar fault. Model 2F features a more

390   complicated moment rate function featuring two peaks of which the first one is reached at t = 0.5

391   s simulation time during simultaneous rupture of both fault planes. The rupture duration of both

392   scenarios is less than 1.5 s. The moment tensor representations of Model 1F and Model 2F are

393   presented in Figure 6c and 6d, respectively. Both scenarios show oblique faulting mechanisms.

394   Model 1F clearly produces a double-couple moment tensor solution (Figure 6c), whereas the

395   Model 2F yields a non-double couple solution due to complex source mechanism (Figure 6d), in

396   agreement with Grigoli et al. (2018). Nevertheless, our simulation produces a smaller amount of

397   CLVD (compensated linear vector dipole) compared to Grigoli et al. (2018). In fact, the equivalent

398   moment tensor solution of Model 2F can be decomposed, following the methodology of Vavryčuk

399   (2015), into 82.95% DC, -5.05% CLVD, and -12% isotropic (ISO) components. In contrast,

400   Grigoli et al. (2018) find -37% CLVD. In our simulations, Model 2F's rupture is characterized by

401   an average rupture speed of $v_r \approx 2{,}250\ m/s$, well below the average Rayleigh wave speed at the

402   depth of the faults ($v_r \sim 0.75 V_S$). The spatial variation of v_r is mainly related to the complexity of

403   rupture around the intersection for both, the main and secondary fault plane. We observe higher

404 average rupture speed $v_r \approx 2,780\ m/s$ ($v_r \sim 0.8V_S$) on the secondary fault plane (see rupture

405 contours every 0.2 s in Figures 5b, 5c). We note the localized occurence of supershear rupture

406 speeds ($\sim 4000\ m/s$) near the edge of the prescribed nucleation patch of the main fault reflecting

407 the high overstress required for initiating the preferred rupture dynamics in our setup. Also, the

408 secondary fault plane features localized supershear episodes ($\sim 3800\ m/s$). In our model setup,

409 this may be translated into locally high fluid overpressure, and/or reflect the low resolution and

410 1D restriction of the used velocity model. More complex fluid effects have been shown to

411 transition sub-rayleigh to supershear ruptures in fully coupled 2D models by Lin and Zoback

412 (2018).

413   In our preferred model, high slip ($\sim 2\ m$) occurs in the center of the main fault. We observe

414 a maximum slip of 1.3 m at the secondary fault plane (Figure 7b). In total, the average on-fault

415 slip is 0.32m. Both, Model 1F and Model 2F, feature higher slip than Song and Lee (2019) infer

416 in their static slip inversion. In addition, differences may arise due to different modeling

417 assumptions in terms of fault dimensions and shear moduli. First, Song and Lee (2019) assume a

418 slightly larger shear modulus of G = 30 GPa than in our model (G = 26 GPa). Second, they assume

419 a single fault plane of significantly larger dimensions (6 x 5 km) than the faults of our models (see

420 section **Fault reconstruction**). This large fault geometry allows for the possibility of near-surface

421 slip.

422   The orientation of fault slip is modulated by the dynamic source process. The dynamic

423 interaction of the two fault planes induces a moderate thrust-faulting component (rake $\sim 135° -$

424 $150°$) on the main fault plane, as well as complex time-dependent rake orientations on the

425 secondary fault (see also Figure 7c, 7d). In contrast to Model 2F, the orientations of the final rake

426 angle of Model 1F are distributed homogeneously, on average at 127°. The rake of Model 1F is

427   different from Model 2F due to different dip angles of the main fault which dips at 43° in Model

428   1F. This average rake angle is comparable to the focal mechanism derived by Grigoli et al. (2018).

429   The average on-fault slip is 0.35 m. We observe that, on average, the rupture speed is $v_r \approx 2400$

430   m/s. Reflecting similar dynamic parameters to Model 2F, Model 1F also experiences supershear

431   rupture near the nucleation patch.

432

433   **Waveform comparison for Model 1F and Model 2F**

434   In the following, we analyze the differences between Model 1F and Model 2F in terms of

435   near and far-field ground motion. Hereinafter, all distances from the fault are considered as Joyner-

436   Boore distances (R_{JB}, the shortest distance from a site to the surface projection of fault planes).

437   We compare synthetic waveforms computed for hypothetical ("virtual") stations located close (~4

438   km) and far (>20 km) from the epicenter.

439   Figure 8b shows three-component waveforms at 19 randomly located virtual stations

440   (Figure 8a). We place 10 stations near the epicenter (~4 km horizontal distance) to inspect near

441   field seismic waveform characteristics. We filter all synthetic waveforms within the frequency

442   band of 0.1 - 2 Hz using a fourth-order Butterworth filter. Figure 8c depicts all 3-component

443   velocity waveforms. Overall, waveforms of scenarios Model 1F and Model 2F are very similar in

444   this frequency range, but waveforms from Model 1F have systematically higher amplitudes than

445   Model 2F. The most remarkable amplitude differences occur on the EW component for stations

446   004, 008, 009, and 010, which are all located above or close to the faults.

447   At some stations, distinct waveform differences appear (e.g., the NS-component of stations

448   007, 014, 011, and 019). Most of these stations are located on the hanging wall. After five seconds,

449   once the rupture is fully arrested, differences vanish, and the waveforms become comparable for

450   both models. As depicted in Figure 8b, the stations located close to the region where faults overlap

451   in Model 2F show significant differences in seismic wave signatures on the horizontal components.

452   One possible explanation may be that the additional secondary fault defocuses ground motions.

453

454   **Off-fault deformation**

455   Our preferred dynamic earthquake rupture model 2F reveals significant off-fault plastic

456   deformation in the vicinity of geometric fault complexity, similar to scenarios of the 1992 Landers

457   earthquake (Wollherr et al., 2018), the 2016 Kaikoura earthquake (Klinger et al., 2019) and the

458   2019 Ridgecrest earthquake sequence (Taufiqurrahman et al., 2019). Here, significant off-fault

459   plastic deformation (quantified as the scalar quantity η following Ma, 2008 and Wollherr et al.,

460   2019) occurs (i) in the pre-existing damage zone at the fault intersection, (ii) at the dilatational side

461   of the main and the secondary fault as expected from previous theoretical and numerical studies,

462   given the shallow angle of both faults and S_{Hmax} (Templeton and Rice, 2008; Gabriel et al., 2013),

463   and (iii) close to the free-surface (see Figures S4c and S4d).

464   The fault intersection of Model 2F elevates the total off-fault plasticity response

465   regularizing high on-fault stresses while limiting peak slip rates and reducing peak ground motions

466   (Andrews 2005; Dunham et al. 2011a; Gabriel et al., 2013; Roten et al., 2014; Wollherr et al.,

467   2018). When comparing waveforms, we indeed notice overall lower velocity amplitudes compared

468   to Model 1F in the surrounding stations of the fault planes caused by the combined effects of fault

469   complexity and off-fault yielding. Interestingly, the stronger plastic yielding response in model 2F

470   leads to lower variability (not shown here) in ground motions (PGV) (as in Wollherr et al., 2019)

471   even though the fault geometry is more complex.

472

473 **Model 1F and Model 2F surface deformations**

474   Next, we compare the co-seismic surface displacement generated by Model 1F to Model

475 2F (Figure 9a, 9b). We translate the synthetic vertical and horizontal displacements into Line-of-

476 sight (LoS) displacement components.

477   The spatial distribution of the co-seismic surface deformations is noticeably different.

478 Model 1F features higher LoS displacements in southeastern direction relative to the Gokgang

479 Fault ($\sim 2\ km$ from the bay) compared to Model 2F ($\sim 5\ km$ from the bay) and generates on

480 average lower negative LoS displacements. Model 1F creates a wider area of uplifted LoS

481 displacements, which resembles an ellipse with a major axis of 6 km and a minor axis of 4.1 km.

482 The most prominent spatial differences are (i) the vertical LoS displacements of Model 1F are

483 slightly migrated to the East relative to the epicenter and (ii) the location of zero displacements in

484 between vertical LoS displacements (in the region of the epicenter) and negative LoS

485 displacements at the eastern-to-southward of the epicenter. Model 2F produces an average of 5 cm

486 subsidence whereas Model 1F only produces 2 cm average subsidence. This can be attributed to

487 Model 1F's more shallow dipping angle. The co-seismic surface displacements of Model 2F

488 compare better than those of Model 1F to InSAR ground deformation inferences of Song and Lee

489 (2019), in terms of the location of the pivot line delimiting positive and negative LoS

490 displacements ($\sim 4.5\ km$ from the bay).

491   While synthetic (Model 2F) and observed surface displacements significantly differ locally

492 and quantitatively, they reveal qualitatively comparable large-scale features. The following

493 observations are captured by Model 2F: (i) Uplift/easting displacement is observed near the

494 epicenter and (ii) the uplifted area forms an ellipse-like shape with a major axis of ~5.6 km and a

495 minor axis of ~3.8 km. Correspondingly, Pohang city also experienced subsidence according to

496   field observations (Kang et al., 2019a, Kang et al., 2019b). Additionally, our synthetics also

497   suggest subsidence underneath the bay.

498   Although the contribution of the secondary fault plane is critical to reproduce the inferred

499   non-DC component, comparison of synthetic co-seismic surface displacements of Model 2F with

500   and without the secondary fault (see Figure S5a) suggests that the contribution of the secondary

501   fault plane to the ground displacement is small (Figure S5b), as expected from its small slip

502   contribution. We note that the InSAR data may not be sensitive enough to discriminate between a

503   one and a two-fault plane model.

504

505   **Model 2F validation by regional waveform modeling**

506   Unfortunately, a local seismic network of eight portable seismic stations (Kim et al., 2018)

507   deployed around the EGS site produced saturated (clipped) seismograms. Therefore, we choose to

508   compare synthetic waveforms to regional recordings at five stations surrounding the Pohang EGS

509   site (see Figure 1) at epicentral distances of approximately 70 km.

510   Model 2F compares well to regional low-frequency seismic wave observations (Figure 8c).

511   Synthetic waveforms are calculated using a Green's function database of teleseismic waveforms

512   (Instaseis, Krischer et al., 2017). We translate the dynamic rupture model into a single moment

513   tensor representation following Ulrich et al. (2019a, 2019b). The Green's function database we

514   use is based on the anisotropic Preliminary Reference Earth Model (PREM), and is accurate to a

515   maximum period of 2 s. Synthetic and observed waveforms are filtered using a 0.033 - 0.08 Hz

516   4th order Butterworth filter, equivalent to the frequency band used in the source inversion of

517   Grigoli et al. (2018). The goodness of fit is assessed by the root-mean-square (rms) misfit.

518   Although the synthetic waveforms compare reasonably well to regional recordings, we find

519   that a few synthetic amplitudes are systematically larger than the observed data. We attribute this

520   to the usage of a 1D PREM model, which is more suitable for modeling synthetics at larger

521   azimuthal distance. Additionally, the fact that our simulation returns a slightly higher seismic

522   moment than observed and is not able to capture the full non-DC component of the source may

523   play a role. In particular, the large misfit at Station TJN on the UD and EW component may be

524   attributed to unmodeled site effects. Our synthetics do not differ significantly from the synthetics

525   of Grigoli et al. (2018), derived by full-waveform inversion of the waveforms recorded at stations

526   BUS2, CHJ2, and NAWB. A significant difference is only noticeable on the NS component of

527   station BUS2 (south of the epicenter, Figure 1).

528

529   Discussion

530   The importance of local stresses for rupture dynamics in EGS

531   The inferences of previous studies vary in terms of stress regimes and maximum horizontal

532   stress orientation around the Pohang EGS site, thereby motivating our systematic numerical

533   experiments as detailed in section **Static and dynamic analysis of initial fault strength and**

534   **stresses** under various loading stress settings. Assuming an Andersonian stress regime, we find

535   that an initial stress state constrained by regional stress inversions is unable to generate the

536   observed thrust-faulting component of the Pohang earthquake. This suggests important local

537   deviations from the regional stress state near the Pohang EGS site. Kim et al. (2017) and Lee et al.

538   (2017) infer the stress orientation at short epicentral distance (< 10 km) from borehole image log

539   data acquired prior to the Pohang earthquake. However, this data is limited to 1 km depth, whereas

540   the Pohang earthquake hypocentral depth is inferred to be deeper, at a depth of 4.27 km. Ellsworth

541   et al. (2019) noted that the in-situ stress state at the Pohang EGS site is transpressional.

542   From our static numerical experiments, we infer that a pure strike-slip stress regime ($s_2 =$

543   s_v) and $S_{Hmax} = 120°$ yield a thrust-faulting component consistent with observations (Figure S2).

544   This finding is corroborated by our dynamic rupture simulations under identical loading (Figure

545   6c, 6d). We also observe that under these conditions spontaneous rupture propagation is favoured.

546   The reverse faulting regime ($s_3 = s_v$) accounting for low $v = 0.1$ was also explored. However,

547   such reverse-stress regime, as suggested by Ellsworth et al. (2019), across the entire fault planes

548   does not yield sufficiently high shear tractions on our fault system - and dynamic rupture dies out

549   quickly.

550   Local variations of the stress state around EGS sites, including the Pohang EGS site, have

551   been observed in hydraulic stimulation experiments of crystalline-rock reservoirs (Schoenball et

552   a., 2010), data-driven geomechanical analysis (Ceunot et al., 2006; Hardebeck and Michael, 2006;

553   Martínez-Garzón et al., 2013; Martínez-Garzón et al. 2014; Schoenball et al., 2014) and numerical

554   experiments (Jeanne et al., 2015; Ziegler et al., 2017). Such spatial and temporal stress

555   reorientation is typically a direct response to hydraulic stimulation and fluid injections (Cornet et

556   al., 2007; Schoenball et al., 2010; Schoenball et al., 2013; Ziegler et al., 2017, Liu and Zahradnik,

557   2019). In the geothermal field surrounding the Geysers in California, Martínez-Garzón et al.

558   (2014) found that the stress regime changed from normal-faulting to strike-slip near the injection

559   wells. At the Pohang EGS site, local variations in the stress regime have been inferred from focal

560   mechanisms of microearthquakes before and after the Pohang earthquake. Woo et al. (2019)

561   reported strike-slip faulting north from the hypocenter to strike-slip associated thrust-faulting and

562   pure thrust-faulting components towards the South before the mainshock. After the mainshock

563   occurred, aftershock focal mechanisms were mainly strike-slip in the SW to oblique faulting in the

564   NE (Kim et al., 2020). Changes in the stress orientation and regime near the hypocenter prior to

565   the mainshock could correspond to hydraulic stimulation and fluid injections (Martínez-Garzón et

566   al., 2014; Liu and Zahradnik, 2019). However, the aftershock source characteristics are probably

567   related to co-seismic stress rotation.

568   Based on our analysis of various numerical experiments, we deduce that our models are

569   highly sensitive to variations in the initial stress state, and therefore allow to finely constrain the

570   fault stress loading parameters. For example, a small change in S_{Hmax} may induce a significant

571   change in the modeled focal mechanism. All faults are exposed to the same local stress regime

572   while experiencing varying ratios of shear and normal loading depending on their orientation

573   towards this loading. Even a small change in fault geometry (e.g., in strike, dip, size, and the angle

574   between fault planes) strongly affects the dynamic rupture result (e.g., Yamashita and Umeda,

575   1994; Aochi et al., 2005; Bhat et al., 2007; Ulrich et al., 2019a; van Zelst et al., 2019), as here

576   illustrated when comparing Model 1F and Model 2F. We point out that trade-offs between the

577   inferred stress state and fault geometry can be readily explored if new observations become

578   available.

579   In summary, these observations support our assumption on the loading stress, which is

580   consistent with Ellsworth et al. (2019) in the nucleation region, but differently oriented everywhere

581   else. Complexities in the in-situ stress state are expected in the region where the Pohang earthquake

582   occurred, due to the history of hydraulic stimulations, that is, the EGS operation itself perturbs the

583   local stress conditions in a manner that makes it more difficult to assess the potential seismic

584   hazard implication (that are usually studied in advance and utilize regional stress information).

585

586 **The importance of critically stressed, static and dynamic weak faults and**

587 **overpressurized fluids**

588 Our experiments (Figure 4) emphasize the necessity of assuming overpressurized fluids

589 ($\gamma > 0.37$) and a close to critical stress state when assuming strong frictional weakening on the

590 fault(s). A critically stressed state has been suggested by Ellsworth et al. (2019) by analyzing

591 dipole sonic logging data at the Pohang drilling site. In our preferred Model 2F, we use the ratio

592 of shear over effective normal stress (τ/σ_n) to quantify fault strength, and find 0.54 and 0.59 for

593 the main and secondary fault plane, respectively. This fault strength is close to the assumed steady-

594 state friction coefficient ($f_0 = 0.6$) which indicates that the faults are close to failure prior to

595 rupture nucleation and thus close to critically stressed.

596 In our preferred model both faults are non-optimally oriented with respect to the local stress

597 conditions. The relative prestress ratio R is 0.35 on the main fault and 0.4 on the secondary fault

598 plane, which is less than our assumed $R_0 = 0.8$. According to Andersonian faulting theory, the fault

599 strength is related to its orientation with respect to the regional stress. Here, the main fault plane

600 is oriented at 54° and the secondary fault at 60° relative to the regional maximum compressive

601 stress ($S_{Hmax} = 77°$). Thus, the two-fault system would be considered weak in the classic, static

602 sense.

603 All modeled faults in this study weaken dramatically at co-seismic slip rates while stress

604 drops are limited by the elevated fluid pressure. Besides resembling the dramatic friction decrease

605 observed in laboratory experiments and the theory of thermal weakening processes, previous

606 dynamic rupture studies utilizing rapid velocity weakening using low values of fully weakened

607 friction coefficient (f_w) reproduced rupture complexities, such as rupture reactivation and pulse-

608 like ruptures, without assuming small-scale heterogeneities (Ulrich et al., 2019a).

609   In our simulation, we use a fluid pressure ratio of 0.5 which corresponds to a reduction of

610   the normal stress of approximately 14.3 MPa compared to a hydrostatic state. The reduction in

611   effective normal stress mechanically lowers the static strength of faults. Our assumption of high

612   fluid pressure may relate to various episodes of drilling mud loss on 30-31 October 2015 at 3800

613   m depth suggesting an increase of fluid pressure on the order of 20 MPa around the borehole, and

614   the fluid injection operations (Ellsworth et al., 2019; Korean Government Commission, 2019).

615

The importance of fault interaction for the dynamic rupture process and faulting mechanism

618   In our preferred model, the secondary fault is only partially ruptured during the Pohang

619   earthquake. Strong variations in slip rate associated with dynamic rupture complexity across the

620   two faults planes and their interaction, spontaneous rupture arrest and the asymmetrically

621   accumulated fault slip on the main and secondary fault plane, could potentially favor dynamic and

622   static Coulomb stress transfers enabling a later activation of the unruptured area of the secondary

623   fault. The largest aftershock that occurred less than three hours after the mainshock at 650 m

624   epicentral distance to the northwest with respect to the mainshock may have occurred in such an

625   unruptured area on the secondary fault.

626   In our model, complex shear faulting across two fault planes induces a non-DC component,

627   which is, nevertheless, considerably smaller (14%) compared to the CLVD component inferred by

628   Grigoli et al. (2018). Additional factors not considered in this study may contribute to an apparent

629   non-DC component, such as strong deviations from fault planarity (larger scale curvature and

630   small-scale roughness, e.g., Bydlon and Dunham, 2015; Shi and Day, 2013; Ulrich and Gabriel,

631   2017; Mai et al., 2018), stronger heterogeneities in fault stress and strength (Ripperger et al., 2008)

632   and 3D subsurface structure (e.g., Pelties et al., 2015) increasing rupture complexity, as well as

633   incorporating tensile faulting, poroelastic rheology, and source or propagation anisotropy (Julian,

634   1998; Boitz et al., 2018). The CLVD contribution may also increase when assuming a larger

635   number of faults. While the limited data available does not suggest rupture of additional fault

636   planes, stochastically distributed and dynamically activated fracture networks (e.g., Okubo et al.

637   2019; Anger and Gabriel, 2019) around the main fault are expected given the on-going stimulation

638   operation.

639

640   **Importance of dense seismic monitoring during EGS projects**

641   The complex interaction of local stress loading and fault strength conditions, rupture

642   dynamics and fault interaction on multiple fault segments presented here highlights the importance

643   of a dense local seismic network within the operational areas for monitoring and analyzing

644   microseismicity before, during, and after EGS operation, to thereby mitigate the potential seismic

645   hazard. Pre-EGS stimulation seismic monitoring is needed to define the 'unperturbed state' of the

646   system (the rock volume to be stimulated) and for characterizing potentially unmapped fault(s)

647   that may interact during cascading rupture; such seismic monitoring may be accompanied by

648   detailed borehole logging to assess the local stress state prior to stimulation.

649   During the stimulation and operational phase, a dense seismic monitoring network is also

650   needed to facilitate high-precision and high-fidelity seismic source studies. In conjunction with

651   detailed operational fluid-injection parameters, the reservoir stress state and its susceptibility for

652   generating earthquakes can be assessed (Galis et al., 2017; Kwiatek et al., 2019). In fact, the

653   available recordings of the operational monitoring seismic network near the Pohang EGS site were

654   saturated (clipped) by the unexpected high magnitude earthquake, thus accelerometers would be

655   useful as complementary instruments in EGS monitoring networks. In addition, the rise of

656   Distributed Acoustic Sensing (DAS) opens new opportunities as an additional seismic monitoring

657   network especially for EGS that is located in urban areas (Zhan, 2019).

658   Our study suggests that fully physics-based numerical simulations prior, during and after

659   an EGS project may be useful to not only gain a first-order understanding of potential effects and

660   consequences of the EGS experiments (e.g., risk-prone area as reflected by peak ground motions

661   (PGVs, Figure S6)), but also to optimally design the seismic monitoring network to ensure that all

662   vital data are collected as needed for future monitoring and mitigation purposes.

663

Conclusions

665   A guided fault reconstruction approach that clusters spatio-temporal aftershock locations

666   accounting for their uncertainty is applied to create a two fault planes dynamic rupture model

667   which reproduces key characteristics of the Pohang earthquake. Rupture complexity is arising from

668   the dynamic interaction of two failing fault planes with shallow intersection angles.

669   Static Mohr-Coulomb failure analysis and 180 numerical simulations demonstrate that the

670   regional loading stress is unable to generate dynamic rupture consistent with the observed faulting

671   style. Resolving the regional tectonic stress field onto one fault of a geometry as suggested by

672   Korean Government Commission (2019), Ellsworth et al. (2019), and Woo et al. (2019) or onto

673   the reconstructed two fault planes leads inevitable to pure strike-slip faulting, in stark contrast to

674   the observed thrust-faulting mechanism. Instead, local stress variation relative to regional stress

675   orientation is needed to generate oblique faulting. We conclude that regional-stress orientation

676   may be misleading when assessing propensity for failure; this has important implications for

677   seismic hazard assessment. Also, overpressurized pore fluids, non-optimally oriented and

678 dynamically weak faults and a close to critical local stress state play major roles for our dynamic

679 rupture models of the Pohang earthquake. Such factors may be assessed when planning and

680 conducting EGS-type experiments, explorations, and operations.

681 Our dynamic rupture simulations reveal dynamic triggering from the main fault plane to

682 the secondary fault plane without direct rupture branching but via "rupture jumping". The

683 preferred two fault plane simulation compares well to regional observed data such as moment

684 release and far-field seismic waveforms. The single fault plane model, on the other hand, is unable

685 to reproduce the observed non-DC focal mechanisms and surface displacement distributions due

686 to simplicity of the dynamic rupture process and a shallower dip angle, respectively. Dynamic fault

687 interaction, amplified by rapid stress changes due to seismic waves reverberating between the two

688 fault planes, are needed to reproduce observations of a strong CLVD component. However, two

689 simultaneously breaking fault planes cannot fully explain the observed source complexity.

690 We demonstrate the maturity and feasibility of high-resolution 3D modeling of rupture

691 dynamics and seismic wave propagation accounting for the complexity of EGS environments and

692 constrained by few observational parameters shedding light on the dynamics of induced and

693 triggered earthquakes. More sophisticated 3D models, fully coupling dynamic earthquake rupture

694 and seismic wave propagation with co-seismic and quasi-static fluid effects, such as poroelasticity,

695 thermal pressurization, pore pressure diffusion, and considering the geometric complexity of

696 networks of fractures and non-planar faults, may allow in future to capture the full physical

697 complexity of nucleation and dynamics of induced earthquakes.

698 In the near future, such physics-based approaches may be synergistically integrated with

699 near-field seismic monitoring before, during, and after EGS operation, thus complementing traffic

700 light systems for hazard and risk mitigation (Bommer et al., 2006; Mignan et al., 2015).

701

Data and resources

703 The open-source software package SeisSol can be downloaded in github repository

704 (https://github.com/SeisSol/SeisSol). All regional waveforms used in this study were

705 downloaded from Incorporated Research Institutions for Seismology (IRIS; https://www.iris.edu

706 (last accessed February 2020)) data management system using FDSN client. PREM anisotropic 2

707 s can be downloaded in the IRIS data services products (http://ds.iris.edu/ds/products/syngine/

708 (last accessed February 2020)). The supplemental for this article provides additional figures, a

709 table, all parameters used for the preferred Model 2F, and a video mentioned in the article. All

710 parameters used for the preferred Model 2F are also available at

711 (https://drive.google.com/open?id=1nm3HZ_YOD-j8t_YatTFfs9prVKplEExj).

712

Acknowledgments

730

References

732   Ahrens, J., B. Geveci, and C. Law, 2005, ParaView: An end-user tool for large-data

733   visualization, in Visualization Handbook, Elsevier Inc., 717–731.

734   Andrews, D. J., 2005, Rupture dynamics with energy loss outside the slip zone, J. Geophys. Res.,

735   110, no. B1, B01307, doi: 10.1029/2004JB003191.

736   Anger, S. and A.-A Gabriel (2019). Dynamic earthquake rupture across complex 3D

737   fracture networks. S55E-0444 presented at 2019 Fall Meeting, AGU, San Francisco, CA, 9-

738   13 Dec.

739   Aochi, H., and R. Madariaga, 2003, The 1999 Izmit, Turkey, earthquake: Nonplanar fault

740   structure, dynamic rupture process, and strong ground motion, Bull. Seismol. Soc. Am., 93,

741   no. 3, 1249–1266, doi: 10.1785/0120020167.

742   Aochi, H., O. Scotti, and C. Berge-Thierry, 2005, Dynamic transfer of rupture across differently

743   oriented segments in a complex 3-D fault system, Geophys. Res. Lett., 32, no. 21, L21304,

744   doi: 10.1029/2005GL024158.

745   Bauer, A., Scheipl, F., Küchenhoff, H., and Gabriel, A.-A. (2018). An introduction to

746   semiparametric function-on-scalar regression. Statistical Modelling, 18(3–4), 346–364.

747   https://doi.org/10.1177/1471082X17748034.

748   Beyreuther, M., R. Barsch, L. Krischer, T. Megies, Y. Behr, and J. Wassermann, 2010, ObsPy: A

749   python toolbox for seismology, Seismol. Res. Lett., 81, no. 3, 530–533, doi:

750   10.1785/gssrl.81.3.530.

751   Bhat, H. S., M. Olives, R. Dmowska, and J. R. Rice, 2007, Role of fault branches in earthquake

752   rupture dynamics, J. Geophys. Res., 112, no. B11, B11309, doi: 10.1029/2007JB005027.

753   Boitz, N., A. Reshetnikov, and S. A. Shapiro, 2018, Visualizing effects of anisotropy on seismic

754   moments and their potency-tensor isotropic equivalent, Geophysics, 83, no. 3, C85–C97,

755   doi: 10.1190/geo2017-0442.1.

756   Bommer, J.J., Oates, S., Cepeda, J.M., Lindholm, C., Bird, J., Torres, R., Marroquín, G. and

757   Rivas, J., 2006. Control of hazard due to seismicity induced by a hot fractured rock

758   geothermal project. Engineering Geology, 83(4), pp.287-306.

759   Breuer, A., A. Heinecke, and M. Bader, 2016, Petascale Local Time Stepping for the ADER-DG

760   Finite Element Method, in Proceedings - 2016 IEEE 30th International Parallel and

761   Distributed Processing Symposium, IPDPS 2016, Institute of Electrical and Electronics

762   Engineers Inc., 854–863.

763   Breuer, A., A. Heinecke, S. Rettenberger, M. Bader, A.-A. Gabriel, and C. Pelties, 2014,

764   Sustained Petascale Performance of Seismic Simulations with SeisSol on SuperMUC, 1–18.

765   Bydlon, S. A., and E. M. Dunham, 2015, Rupture dynamics and ground motions from

766   earthquakes in 2-D heterogeneous media, Geophys. Res. Lett., 42, no. 6, 1701–1709, doi:

767   10.1002/2014GL062982.

768   Cappa, F., and J. Rutqvist, 2012, Seismic rupture and ground accelerations induced by CO_2

769   injection in the shallow crust, Geophys. J. Int., 190, no. 3, 1784–1789, doi: 10.1111/j.1365-

770   246X.2012.05606.x.

771   Chang, K. W., H. Yoon, Y. Kim, and M. Y. Lee, 2020, Operational and geological controls of

772   coupled poroelastic stressing and pore-pressure accumulation along faults: Induced

773   earthquakes in Pohang, South Korea, Sci. Rep., 10, no. 1, 2073, doi: 10.1038/s41598-020-

774   58881-z.

775   Cheng, Y., and X. Chen, 2018, Characteristics of seismicity inside and outside the salton sea

776   geothermal field, Bull. Seismol. Soc. Am., 108, no. 4, 1877–1888, doi:

777   10.1785/0120170311.

778   Choi, J. H., K. Ko, Y. S. Gihn, C. S. Cho, H. Lee, S. G. Song, E. S. Bang, H. J. Lee, H. K. Bae,

779   S. W. Kim et al., 2019, Surface deformations and rupture processes associated with the

780   2017 Mw 5.4 Pohang, Korea, earthquake, Bull. Seismol. Soc. Am., 109, no. 2, 756–769,

781   doi: 10.1785/0120180167.

782   Cornet, F.H., T. Bérard, and S. Bourouis, 2007. How close to failure is a granite rock mass at a 5

783   km depth?. International Journal of Rock Mechanics and Mining Sciences, 44(1), pp.47-66.

784   Cuenot, N., J. Charléty, L. Dorbath, and H. Haessler, 2006, Faulting mechanisms and stress

785   regime at the European HDR site of Soultz-sous-Forêts, France, Geothermics, 35, nos. 5–6,

786   561–575, doi: 10.1016/j.geothermics.2006.11.007.

787   Dieterich, J. H., K. B. Richards-Dinger, and K. A. Kroll, 2015, Modeling injection-induced

788   seismicity with the physics-based earthquake simulator RSQSim, Seismol. Res. Lett., 86,

789   no. 4, 1102–1109, doi: 10.1785/0220150057.

790   Duan, B., 2016, Spontaneous rupture on natural fractures and seismic radiation during hydraulic

791   fracturing treatments, Geophys. Res. Lett., 43, no. 14, 7451–7458, doi:

792   10.1002/2016GL069083.

793   Dumbser, M., and M. Käser, 2006, An arbitrary high-order discontinuous Galerkin method for

794   elastic waves on unstructured meshes - II. The three-dimensional isotropic case, Geophys. J.

795   Int., 167, no. 1, 319–336, doi: 10.1111/j.1365-246X.2006.03120.x.

796   Dunham, E. M., D. Belanger, L. Cong, and J. E. Kozdon, 2011a, Earthquake ruptures with

797   strongly rate-weakening friction and off-fault plasticity, part 1: Planar faults, Bull. Seismol.

798   Soc. Am., 101, no. 5, 2296–2307, doi: 10.1785/0120100075.

799   Dunham, E. M., D. Belanger, L. Cong, and J. E. Kozdon, 2011b, Earthquake ruptures with

800   strongly rate-weakening friction and off-fault plasticity, part 2: Nonplanar faults, Bull.

801   Seismol. Soc. Am., 101, no. 5, 2308–2322, doi: 10.1785/0120100076.

802   Ellsworth, W. L., D. Giardini, J. Townend, S. Ge, and T. Shimamoto, 2019, Triggering of the

803   Pohang, Korea, Earthquake (Mw 5.5) by enhanced geothermal system stimulation,

804   Seismological Society of America, 1844–1858.

805   Emerson paradigm holding, 2018, GoCad: A computer aided design program for geological

806   applications.

807   Gabriel, A.-A., J.-P. Ampuero, L. A. Dalguer, and P. M. Mai, 2013, Source properties of

808   dynamic rupture pulses with off-fault plasticity, J. Geophys. Res. Solid Earth, 118, no. 8,

809   4117–4126, doi: 10.1002/jgrb.50213.

810   Galis, M., J. P. Ampuero, P. M. Mai, and F. Cappa, 2017, Induced seismicity provides insight

811   into why earthquake ruptures stop, Sci. Adv., 3, no. 12, doi: 10.1126/sciadv.aap7528.

812   Gallovič, F., Valentová, Ľ., Ampuero, J.-P., and Gabriel, A.-A. , 2019a. Bayesian dynamic finite-

813   fault inversion: 1. Method and synthetic test. J. Geophys. Res., 124, 6949– 6969.

814   https://doi.org/10.1029/2019JB017510

815   Gallovič, F., Valentová, Ľ., Ampuero, J.-P., and Gabriel, A.-A., 2019b. Bayesian Dynamic

816   Finite-Fault Inversion: 2. Application to the 2016 Mw6.2 Amatrice, Italy, Earthquake, J.

817   Geophys. Res., doi:10.1029/2019JB017512.

818   Garagash, D. I., and L. N. Germanovich, 2012, Nucleation and arrest of dynamic slip on a

819   pressurized fault, J. Geophys. Res. B Solid Earth, 117, no. 10, doi: 10.1029/2012JB009209.

820   Grigoli, F., S. Cesca, A. P. Rinaldi, A. Manconi, J. A. López-Comino, J. F. Clinton, R.

821   Westaway, C. Cauzzi, T. Dahm, and S. Wiemer, 2018, The November 2017 M w 5.5

822   Pohang earthquake: A possible case of induced seismicity in South Korea, Science (80-.).,

823   360, no. 6392, 1003–1006, doi: 10.1126/science.aat2010.

824   Happ, C., Scheipl, F., A.-A. Gabriel, S. Greven, 2019, A general framework for multivariate

825   functional principal component analysis of amplitude and phase variation. Stat. 2019;

826   8:e220. https://doi.org/10.1002/sta4.220

827   Hardebeck, J. L., and A. J. Michael, 2006, Damped regional-scale stress inversions:

828   Methodology and examples for southern California and the Coalinga aftershock sequence,

829   J. Geophys. Res. Solid Earth, 111, no. B11, doi: 10.1029/2005JB004144.

830   Harris, R. A., M. Barall, B. Aagaard, S. Ma, D. Roten, K. Olsen, B. Duan, D. Lie, B. Luo, K. Bai

831   et al., 2018, A suite of exercises for verifying dynamic earthquake rupture codes, Seismol.

832   Res. Lett., 89, no. 3, 1146–1162, doi: 10.1785/0220170222.

833   Harris, R. A., M. Barall, D. J. Andrews, B. Duan, S. Ma, E. M. Dunham, A.-A. Gabriel, Y.

834   Kaneko, Y. Kase, B. T. Aagaard et al., 2011, Verifying a Computational Method for

835   Predicting Extreme Ground Motion, Seismol. Res. Lett., 82, no. 5, 638–644, doi:

836   10.1785/gssrl.82.5.638.

837   Heidbach, O. M. Rajabi, X. Cui, K. Fuchs, B. Muller, J. Reinecker, K. Reiter, M. Tingay, F.

838   Wenzel, F. Xie, et al., 2018, The World Stress Map database release 2016: Crustal stress

839   pattern across scales, Elsevier B.V., 484–498.

840   Heinecke, A., A. Breuer, S. Retenberger, M. Bader, A.-A. Gabriel, C. Pelties, A. Bode, W.

841   Barth, X. Liao, K. Vaidyanathan, et al., 2014, Petascale High Order Dynamic Rupture

842   Earthquake Simulations on Heterogeneous Supercomputers, in International Conference for

843   High Performance Computing, Networking, Storage and Analysis, SC, IEEE Computer

844   Society, 3–14.

845   Hirata, T., 1989, Fractal dimension of fault systems in Japan: Fractal structure in rock fracture

846   geometry at various scales, Pure Appl. Geophys. PAGEOPH, 131, nos. 1–2, 157–170, doi:

847   10.1007/BF00874485.

848   Hofmann, H., G. Zimmermann, M. Farkas, E. Huenges, A. Zang, M. Leonhardt, G. Kwiatek, P.

849   Martinez-Garzon, M. Bohnhoff, K. B. Min et al., 2019, First field application of cyclic soft

850   stimulation at the Pohang Enhanced Geothermal System site in Korea, Geophys. J. Int.

851   (2019) 217, 926–949

852   Hunter, J. D., 2007, Matplotlib: A 2D graphics environment, Comput. Sci. Eng., 9, no. 3, 99–

853   104, doi: 10.1109/MCSE.2007.55.

854   Jeanne, P., J. Rutqvist, P. F. Dobson, J. Garcia, M. Walters, C. Hartline, and A. Borgia, 2015,

855   Geomechanical simulation of the stress tensor rotation caused by injection of cold water in a

856   deep geothermal reservoir, J. Geophys. Res. Solid Earth, 120, no. 12, 8422–8438, doi:

857   10.1002/2015JB012414.

858   Jin, L., and M. D. Zoback, 2018, Fully Dynamic Spontaneous Rupture Due to Quasi-Static Pore

859   Pressure and Poroelastic Effects: An Implicit Nonlinear Computational Model of Fluid-

860   Induced Seismic Events, J. Geophys. Res. Solid Earth, 123, no. 11, 9430–9468, doi:

861   10.1029/2018JB015669.

862   Julian, B. R., A. D. Miller, and G. R. Foulger, 1998, Non-double-couple earthquakes 1. Theory,

863   Rev. Geophys., 36, no. 4, 525–549, doi: 10.1029/98RG00716.

864   Kang, S., B. Kim, S. Bae, H. Lee, and M. Kim, 2019a, Earthquake-Induced Ground

865   Deformations in the Low-Seismicity Region: A Case of the 2017 M5.4 Pohang, South

866   Korea, Earthquake, Earthq. Spectra, 35, no. 3, 1235–1260, doi: 10.1193/062318EQS160M.

867   Kang, S., B. Kim, H. Cho, J. Lee, K. Kim, S. Bae, and C. Sun, 2019b, Ground-Motion

868   Amplifications in Small-Size Hills: Case Study of Gokgang-ri, South Korea, during the

869   2017 ML 5.4 Pohang Earthquake Sequence, Bull. Seismol. Soc. Am., 109, no. 6, 2626–

870   2643, doi: 10.1785/0120190064.

871   Käser, M., and M. Dumbser, 2006, An arbitrary high-order discontinuous Galerkin method for

872   elastic waves on unstructured meshes - I. The two-dimensional isotropic case with external

873   source terms, Geophys. J. Int., 166, no. 2, 855–877, doi: 10.1111/j.1365-

874   246X.2006.03051.x.

875   Kim, K. H., J. H. Ree, Y. H. Kim, S. Kim, S. Y. Kang, and W. Seo, 2018, Assessing whether the

876   2017 Mw5.4 Pohang earthquake in South Korea was an induced event, Science (80-.)., 360,

877   no. 6392, 1007–1009, doi: 10.1126/science.aat6081.

878   Kim, K. H., W. Seo, J. Han, J. Kwon, S. Y. Kang, J. H. Ree, S. Kim, and K. Liu, 2020, The 2017

879   ML 5.4 Pohang earthquake sequence, Korea, recorded by a dense seismic network,

880   Tectonophysics, 774, doi: 10.1016/j.tecto.2019.228306.

881   Kim, H., L. Xie, K. B. Min, S. Bae, and O. Stephansson, 2017, Integrated In Situ Stress

882   Estimation by Hydraulic Fracturing, Borehole Observations and Numerical Analysis at the

883   EXP-1 Borehole in Pohang, Korea, Rock Mech. Rock Eng., 50, no. 12, 3141–3155, doi:

884   10.1007/s00603-017-1284-1.

885   Klinger, Y., K. Okubo, A. Vallage, J. Champenois, A. Delorme, E. Rougier, Z. Lei, E. E. Knight,

886   A. Munjiza, C. Satriano, et al., 2018, Earthquake Damage Patterns Resolve Complex

887   Rupture Processes, Geophys. Res. Lett., 45, no. 19, 10,279-10,287, doi:

888   10.1029/2018GL078842.

889   Korean Government Commission, 2019, Summary Report of the Korean Government

890   Commission on Relations between the 2017 Pohang Earthquake and EGS Project.

891   Krischer, L., A. R. Hutko, M. Van Driel, S. Stähler, M. Bahavar, C. Trabant, and T. Nissen-

892   Meyer, 2017, On-demand custom broadband synthetic seismograms, Seismol. Res. Lett.,

893   88, no. 4, 1127–1140, doi: 10.1785/0220160210.

894   Kroll, K. A., K. B. Richards-Dinger, and J. H. Dieterich, 2017, Sensitivity of Induced Seismic

895   Sequences to Rate-and-State Frictional Processes, J. Geophys. Res. Solid Earth, 122, no. 12,

896   10,207-10,219, doi: 10.1002/2017JB014841.

897   Kwiatek, G., T. Saarno, T. Ader, F. Bluemle, M. Bohnhoff, M. Chendorain, G. Dresen, P.

898   Heikkinen, I. Kukkonen, P. Leary et al., 2019, Controlling fluid-induced seismicity during a

899   6.1-km-deep geothermal stimulation in Finland, Sci. Adv., 5, no. 5, eaav7224, doi:

900   10.1126/sciadv.aav7224.

901   Kyriakopoulos, C., D. D. Oglesby, T. K. Rockwell, A. J. Meltzner, M. Barall, J. M. Fletcher, and

902   D. Tulanowski, 2019, Dynamic Rupture Scenarios in the Brawley Seismic Zone, Salton

903   Trough, Southern California, J. Geophys. Res. Solid Earth, 124, no. 4, 3680–3707, doi:

904   10.1029/2018JB016795.

905   de la Puente, J., J.-P. Ampuero, and M. Käser, 2009, Dynamic rupture modeling on unstructured

906   meshes using a discontinuous Galerkin method, J. Geophys. Res., 114, no. B10, B10302,

907   doi: 10.1029/2008JB006271.

908   Lee, K. K., W. L. Ellsworth, D. Giardini, J. Townend, S. Ge, T. Shimamoto, I. W. Yeo, T. S.

909   Kang, J. Rhie, D. G. Sheen et al., 2019, Managing injection-induced seismic risks, Science,

910   364, no. 6442, 730–732, doi: 10.1126/science.aax1878.

911   Lee, J., T. K. Hong, and C. Chang, 2017, Crustal stress field perturbations in the continental

912   margin around the Korean Peninsula and Japanese islands, Tectonophysics, 718, 140–149,

913   doi: 10.1016/j.tecto.2017.08.003.

914   Lee, H., Y. J. Shinn, S. H. Ong, S. W. Woo, K. G. Park, T. J. Lee, and S. W. Moon, 2017, Fault

915   reactivation potential of an offshore CO2 storage site, Pohang Basin, South Korea, J. Pet.

916   Sci. Eng., 152, 427–442, doi: 10.1016/j.petrol.2017.03.014.

917   Liu, J. and Zahradník, J., The 2019 MW 5.7 Changning earthquake, Sichuan Basin, China–a

918   shallow doublet with different faulting styles. Geophys. Res. Let., p.e2019GL085408.

919   Ma, S., 2008, A physical model for widespread near-surface and fault zone damage induced by

920   earthquakes. *Geochemistry, Geophysics, Geosystems*, *9*(11).

921   Mai, P. M., M. Galis, K. K. S. Thingbaijam, J. C. Vyas, and E. M. Dunham, 2018, Accounting

922   for Fault Roughness in Pseudo-Dynamic Ground-Motion Simulations, Birkhäuser, Cham,

923   95–126.

924   Martínez-Garzón, P., M. Bohnhoff, G. Kwiatek, and G. Dresen, 2013, Stress tensor changes

925   related to fluid injection at The Geysers geothermal field, California, Geophys. Res. Lett.,

926   40, no. 11, 2596–2601, doi: 10.1002/grl.50438.

927   Martínez-Garzón, P., G. Kwiatek, H. Sone, M. Bohnhoff, G. Dresen, and C. Hartline, 2014,

928   Spatiotemporal changes, faulting regimes, and source parameters of induced seismicity: A

929   case study from The Geysers geothermal field, J. Geophys. Res. Solid Earth, 119, no. 11,

930   8378–8396, doi: 10.1002/2014JB011385.

931 McGarr, A., 2014, Maximum magnitude earthquakes induced by fluid injection, J. Geophys.

932   Res. Solid Earth, 119, no. 2, 1008–1019, doi: 10.1002/2013JB010597.

933 Mignan, A., Landtwing, D., Kästli, P., Mena, B. and Wiemer, S., 2015. Induced seismicity risk

934   analysis of the 2006 Basel, Switzerland, Enhanced Geothermal System project: Influence of

935   uncertainties on risk mitigation. *Geothermics*, *53*, pp.133-146.

936 Okubo, K., H. S. Bhat, E. Rougier, S. Marty, A. Schubnel, Z. Lei, E. E. Knight, and Y. Klinger,

937   2019, Dynamics, Radiation, and Overall Energy Budget of Earthquake Rupture With

938   Coseismic Off-Fault Damage, J. Geophys. Res. Solid Earth, 124, no. 11, 11771–11801, doi:

939   10.1029/2019JB017304.

940 Pelties, C., A.-A. Gabriel, and J.-P. Ampuero, 2014, Verification of an ADER-DG method for

941   complex dynamic rupture problems, Geosci. Model Dev., 7, no. 3, 847–866, doi:

942   10.5194/gmd-7-847-2014 and Geoscientific Model Development Discussions, 6(4), 5981--

943   6034, doi:10.5194/gmdd-6-5981-2013.

944 Pelties, C., Y. Huang, and J. P. Ampuero, 2015, Pulse-Like Rupture Induced by Three-

945   Dimensional Fault Zone Flower Structures, Pure Appl. Geophys., 172, no. 5, 1229–1241,

946   doi: 10.1007/s00024-014-0881-0.

947 Pelties, C., J. de la Puente, J.-P. Ampuero, G. B. Brietzke, and M. Käser, 2012, Three-

948   dimensional dynamic rupture simulation with a high-order discontinuous Galerkin method

949   on unstructured tetrahedral meshes, J. Geophys. Res. Solid Earth, 117, no. B2, n/a-n/a, doi:

950   10.1029/2011JB008857.

951   Peyrat, S., K. Olsen, and R. Madariaga, 2001, Dynamic modeling of the 1992 Landers

952   earthquake, J. Geophys. Res. Solid Earth, 106, no. B11, 26467–26482, doi:

953   10.1029/2001jb000205.

954   Rettenberger, S., O. Meister, M. Bader, and A. A. Gabriely, 2016, ASAGI - A parallel server for

955   adaptive geoinformation, in ACM International Conference Proceeding Series, Association

956   for Computing Machinery.

957   Richards-Dinger, K., and J. H. Dieterich, 2012, RSQSim earthquake simulator, Seismol. Res.

958   Lett., 83, no. 6, 983–990, doi: 10.1785/0220120105.

959   Ripperger, J., Mai, P.M. and Ampuero, J.P., 2008. Variability of near-field ground motion from

960   dynamic earthquake rupture simulations. *Bulletin of the seismological society of America*,

961   *98*(3), pp.1207-1228.

962   Roten, D., K. B. Olsen, S. M. Day, Y. Cui, and D. Fäh, 2014, Expected seismic shaking in Los

963   Angeles reduced by San Andreas fault zone plasticity, Geophys. Res. Lett., 41, no. 8, 2769–

964   2777, doi: 10.1002/2014GL059411.

965   Schoenball, M., L. Dorbath, E. Gaucher, J. F. Wellmann, and T. Kohl, 2014, Change of stress

966   regime during geothermal reservoir stimulation, Geophys. Res. Lett., 41, no. 4, 1163–1170,

967   doi: 10.1002/2013GL058514.

968   Schoenball, M., T. M. Müller, B. I. R. Müller, and O. Heidbach, 2010, Fluid-induced

969   microseismicity in pre-stressed rock masses, Geophys. J. Int., 180, no. 2, 813–819, doi:

970   10.1111/j.1365-246X.2009.04443.x.

971   Shi, Z., and S. M. Day, 2013, Rupture dynamics and ground motion from 3-D rough-fault

972   simulations, J. Geophys. Res. Solid Earth, 118, no. 3, 1122–1141, doi: 10.1002/jgrb.50094.

973   Simmetrix Inc, 2017, SimModeler: Simulation modeling suite 14.0 documentation (Tech. Rep.).

974   Soh, I., C. Chang, J. Lee, T.-K. Hong, and E.-S. Park, 2018, Tectonic stress orientations and

975   magnitudes, and friction of faults, deduced from earthquake focal mechanism inversions

976   over the Korean Peninsula, Geophys. J. Int., 213, no. 2, 1360–1373, doi:

977   10.1093/gji/ggy061.

978   Song, S. G., and H. Lee, 2019, Static slip model of the 2017 M w 5.4 Pohang, South Korea,

979   earthquake constrained by the InSAR data, Seismol. Res. Lett., 90, no. 1, 140–148, doi:

980   10.1785/0220180156.

981   Di Toro, G., R. Han, T. Hirose, N. De Paola, S. Nielsen, K. Mizoguchi, F. Ferri, M. Cocco, and

982   T. Shimamoto, 2011, Fault lubrication during earthquakes, Nature, 471, no. 7339, 494–499,

983   doi: 10.1038/nature09838.

984   Taufiqurrahman, T., A.-A. Gabriel, B. Li, D. Li, S. A. Wirp, T. Ulrich, K. H. Palgunadi, A.

985   Verdecchia, S. Carena, and Z. K. Mildon, 2019, High-resolution integrated dynamic rupture

986   modeling of the 2019 M6. 4 Searles Valley and M7. 1 Ridgecrest earthquakes. S31G-0487

987   presented at 2019 Fall Meeting, AGU, San Francisco, CA, 9-13 Dec.

988   Templeton, E.L. and Rice, J.R., 2008. Off-fault plasticity and earthquake rupture dynamics: 1.

989   Dry materials or neglect of fluid pressure changes. J. Geophys. Res.: Solid Earth, 113(B9).

990   Ulrich, T., and A.-A. Gabriel, 2017, 3D fault curvature and fractal roughness: Insights for

991   rupture dynamics and ground motions using a Discontinuous Galerkin method. In EGU

992   General Assembly Conference Abstract, Vol. 19, Vienna, Austria, pp. 18689.

993   Ulrich, T., A. A. Gabriel, J. P. Ampuero, and W. Xu, 2019a, Dynamic viability of the 2016 Mw

994   7.8 Kaikōura earthquake cascade on weak crustal faults, Nat. Commun., 10, no. 1, doi:

995   10.1038/s41467-019-09125-w.

996   Ulrich, T., S. Vater, E. H. Madden, J. Behrens, Y. van Dinther, I. van Zelst, E. J. Fielding, C.

997   Liang, and A. A. Gabriel, 2019b, Coupled, Physics-Based Modeling Reveals Earthquake

998   Displacements are Critical to the 2018 Palu, Sulawesi Tsunami, Pure Appl. Geophys., 176,

999   no. 10, 4069–4109, doi: 10.1007/s00024-019-02290-5.

1000   Uphoff, C. and Bader, M., 2016, July. Generating high performance matrix kernels for

1001   earthquake simulations with viscoelastic attenuation. In 2016 International Conference on

1002   High Performance Computing and Simulation (HPCS) (pp. 908-916). IEEE.

1003   Uphoff, C., S. Rettenberger, M. Bader, E. H. Madden, T. Ulrich, S. Wollherr, and A.-A. Gabriel,

1004   2017, Extreme scale multi-physics simulations of the tsunamigenic 2004 sumatra

1005   megathrust earthquake, Proc. Int. Conf. High Perform. Comput. Networking, Storage Anal.

1006   - SC '17, no. November, 1–16, doi: 10.1145/3126908.3126948.

1007   Vavryčuk, V., 2015, Moment tensor decompositions revisited, J. Seismol., 19, no. 1, 231–252,

1008   doi: 10.1007/s10950-014-9463-y.

1009   Viesca, R. C., and J. R. Rice, 2012, Nucleation of slip-weakening rupture instability in landslides

1010   by localized increase of pore pressure, J. Geophys. Res. Solid Earth, 117, no. 3, doi:

1011   10.1029/2011JB008866.

1012   Wang, Y., G. Ouillon, J. Woessner, D. Sornette, and S. Husen, 2013, Automatic reconstruction

1013   of fault networks from seismicity catalogs including location uncertainty, J. Geophys. Res.

1014   Solid Earth, 118, no. 11, 5956–5975, doi: 10.1002/2013JB010164.

1015   Wessel, P., W. H. F. Smith, R. Scharroo, J. Luis, and F. Wobbe, 2013, Generic Mapping Tools:

1016   Improved Version Released, Eos, Trans. Am. Geophys. Union, 94, no. 45, 409–410, doi:

1017   10.1002/2013EO450001.

1018   Wolf, Sebastian, A.-A. Gabriel, and M. Bader, 2020, Optimisation and Local Time Stepping of

1019   an ADER-DG Scheme for Fully Anisotropic Wave Propagation in Complex Geometries, in

1020   Proceedings of the 10th International Workshop on Advances in High-Performance

1021   Computational Earth Sciences: Applications and Frameworks, preprint available at

1022   https://wolke.geophysik.uni-muenchen.de/s/ReaBg7mjabPwwLk#pdfviewer.

1023   Wollherr, S., A. Gabriel, and P. M. Mai, 2019, Landers 1992 "Reloaded": Integrative Dynamic

1024   Earthquake Rupture Modeling, J. Geophys. Res. Solid Earth, 124, no. 7, 6666–6702, doi:

1025   10.1029/2018JB016355.

1026   Wollherr, S., A. A. Gabriel, and C. Uphoff, 2018, Off-fault plasticity in three-dimensional

1027   dynamic rupture simulations using a modal Discontinuous Galerkin method on unstructured

1028   meshes: Implementation, verification and application, Geophys. J. Int., 214, no. 3, 1556–

1029   1584, doi: 10.1093/GJI/GGY213.

1030   Woo, J. -U., M. Kim, D. -H. Sheen, T. -S. Kang, J. Rhie, F. Grigoli, W. L. Ellsworth, and D.

1031   Giardini, 2019, An In-Depth Seismological Analysis Revealing a Causal Link Between the

1032   2017 M $_W$ 5.5 Pohang Earthquake and EGS Project, J. Geophys. Res. Solid Earth,

1033   2019JB018368, doi: 10.1029/2019JB018368.

1034   Yamashita, T., and Y. Umeda, 1994, Earthquake rupture complexity due to dynamic nucleation

1035   and interaction of subsidiary faults, Pure Appl. Geophys. PAGEOPH, 143, nos. 1–3, 89–

1036   116, doi: 10.1007/BF00874325.

1037   Zaliapin, I., and Y. Ben-Zion, 2013, Earthquake clusters in southern California I: Identification

1038   and stability, J. Geophys. Res. Solid Earth, 118, no. 6, 2847–2864, doi: 10.1002/jgrb.50179.

1039   van Zelst, I., S. Wollherr, A. -A. Gabriel, E. H. Madden, and Y. Dinther, 2019, Modeling

1040   Megathrust Earthquakes Across Scales: One-way Coupling From Geodynamics and

1041   Seismic Cycles to Dynamic Rupture, J. Geophys. Res. Solid Earth, 124, no. 11, 11414–

1042   11446, doi: 10.1029/2019JB017539.

1043   Zhan, Z., 2019, Distributed acoustic sensing turns fiber-optic cables into sensitive seismic

1044   antennas, Seismol. Res. Lett., 91, no. 1, 1–15, doi: 10.1785/0220190112.

1045   Zhang, Q., and P. M. Shearer, 2016, A new method to identify earthquake swarms applied to

1046   seismicity near the San Jacinto Fault, California, Geophys. J. Int., 205, no. 2, 995–1005,

1047   doi: 10.1093/gji/ggw073.

1048   Ziegler, M. O., O. Heidbach, A. Zang, P. Martínez-Garzón, and M. Bohnhoff, 2017, Estimation

1049   of the differential stress from the stress rotation angle in low permeable rock, Geophys. Res.

1050   Lett., 44, no. 13, 6761–6770, doi: 10.1002/2017GL073598.

1051

1052   **FULL AUTHOR'S MAILING LIST:**

1053   Kadek Hendrawan Palgunadi   : kadek.palgunadi@kaust.edu.sa

1054   Alice-Agnes Gabriel   : gabriel@geophysik.uni-muenchen.de

1055   Thomas Ulrich   : ulrich@geophysik.uni-muenchen.de

1056   José Ángel Lopéz-Comino   : lopezcomino@uni-potsdam.de

1057   Paul Martin Mai   : martin.mai@kaust.edu.sa

1058

1059   **LIST OF TABLE CAPTIONS:**

1060   **Table A1**. Fault friction parameters assumed in this study

1061

1062   **LIST OF FIGURE CAPTIONS:**

1063   **Figure 1.** Map of the South Korean Peninsula showing the near-regional broadband stations (blue

1064   triangles). Solid and dashed lines represent the Yangsan and interpreted geological faults near the

1065   Pohang EGS site, respectively. The two inset plots present the location and geometry of the faults

1066   of Model 1F (upper panel) and Model 2F (lower panel). The thicker black lines mark the near-

1067   surface edge of the fault planes. Colored dots depict aftershocks locations extracted from Kim et

1068   al. (2018). The non-double-couple solution of Grigoli et al. (2018) is also shown.

1069

1070   **Figure 2**. Fault reconstruction using guided anisotropic location uncertainty distribution (g-

1071   ACLUD). a) Spatiotemporal density plot of the mainshock and aftershocks based on the nearest-

1072   neighbor distance. b), c) and d) Two fault plane geometry inferred by the g-ACLUD method. The

1073   main fault plane has a strike of 214° and dips at 65°, while the secondary fault plane has a strike

1074   199° and dips at 60°. Black dots depict the seismicity used in this study. The geometry of the faults

1075   is shown in views b) as view from North, in c) as view from South, and d) in map view. The red

1076   star denotes the hypocenter of the Pohang earthquake.

1077

1078   **Figure 3**. 3D rendering of the unstructured tetrahedral computational mesh, and the fault plane

1079   with final slip on the 2-fault preferred model (Model 2F) of the Pohang earthquake (warm colors,

1080   in m), and the radiated seismic wavefield 5 seconds after rupture initiation (cold colors, absolute

1081   particle velocity in m/s). Note the strong effect of the high-resolution topography on modulating

1082   the seismic wavefield.

1083

1084   **Figure 4**. Graphical summary of the outcome of 180 dynamic rupture simulations assuming

1085   different combinations of initial relative prestress ratio (R_0), fluid-pressure ratio (γ) and direction

1086   of S_{Hmax}. The corresponding 180 square frames are filled with color if the combination of

1087   parameters is able to trigger self-sustained rupture beyond the nucleation region on any fault. The

1088 S_{Hmax} direction is indicated by the size of the frame, leading to six imbricated frames for each set

1089   of prestress and fluid-pressure ratio parameters.

1090

1091   **Figure 5**. Overview of the simulated earthquake rupture of the preferred model (Model 2F),

1092   showing in a) and b) the space-time evolutions of the absolute slip-rate (in m/s) across the main

1093   and secondary fault plane. a) (left panel) view from North displaying the main fault rupture.

1094   Snapshots every 0.1 s. (right panel) view from South highlighting the rupture of a portion of the

1095   secondary fault. Snapshots every 0.05 s. b-c) Rupture-time contours at intervals of 0.2 s.

1096

1097   **Figure 6**. Moment rate release of a) Model 1F and b) Model 2F and moment tensor

1098   representation of the preferred one-fault c) and two-fault d) models.

1099

1100   **Figure 7**. Distribution of absolute fault slip (in m) in a) and b), and rake angles (in degrees) in c)

1101   and d) for the preferred dynamic rupture scenario (Model 2F) a) and c) view from North

1102   highlighting the main fault rupture. b) and d) view from South highlighting the rupture of a portion

1103   of the secondary fault. The white star in panel a) marks the considered hypocenter location.

1104

1105   **Figure 8**. Comparison of synthetic and observed ground motion waveforms. a) Distribution of

1106   virtual stations (green triangles) at which synthetic waveforms are compared in b). The beachball

1107   is the moment tensor representation of the preferred 2 planes model scenario (Model 2F). Solid

1108   and dashed red lines represent the mapped Yangsan fault surface trace and the interpreted fault

1109   traces near the Pohang EGS site, respectively. The two rectangles show the location and geometry

1110   of the faults used in this study. b) Comparison of synthetic waveforms using one (Model 1F, blue

1111   dashed lines) and two fault planes (Model 2F, red solid lines) at the 19 dummy stations located in

1112   a). A 0.1 - 2 Hz 4th order Butterworth filter is applied to all traces. All traces are normalized. For

1113   each trace, the maximum velocity amplitude (in m/s) of Model 1F is indicated within a black

1114   square. c) Observed (black) and synthetic (red) waveforms for five regional stations for up-down

1115   (UD), east-west (EW) and north-south (NS) components (all located in South Korea, see blue

1116   triangles in Figure 1). t = 0 s denotes the origin time of the Pohang earthquake. A 0.033-0.08 Hz

1117 4th order Butterworth filter is applied to all traces. Synthetic regional waveforms are generated

1118   from the preferred dynamic rupture scenario Model 2F using Instaseis (Krischer et al., 2017) and

1119   2 s accurate Green's functions based on the PREM anisotropic model.

1120

1121   **Figure 9**. ((a) and (b)) Co-seismic surface displacements in the InSAR Line-of-sight (LoS)

1122   direction (in m) generated by a) Model 1F; one-plane (rectangle) and b) Model 2F; two-planes

1123   (two rectangles) preferred dynamic rupture scenario, respectively. The dashed red lines represent

1124   the traces of the interpreted faults near the EGS site.

1125

1126   **LIST OF TABLES:**

1127   **Table A1**. Fault friction parameters assumed in this study

Parameter	Symbol	Value
Direct effect parameter	a	0.01 - 0.02 z≤3.3 km and 0.01 z > 3.3 km
Evolution effect parameter	b	0.014
Reference slip velocity	V_0	10^{-6}m/s
Steady-state friction coefficient at V_0	f_0	0.6
State-evolution distance	L	0.2 m
Weakening slip velocity	V_W	0.1 - 1.0 z≤3.3 km and 0.1 z > 3.3 km
Fully weakened friction coefficient	f_W	0.1
Initial slip rate	V_{ini}	10^{-16}m/s

1128

1129   **LIST OF FIGURES:**
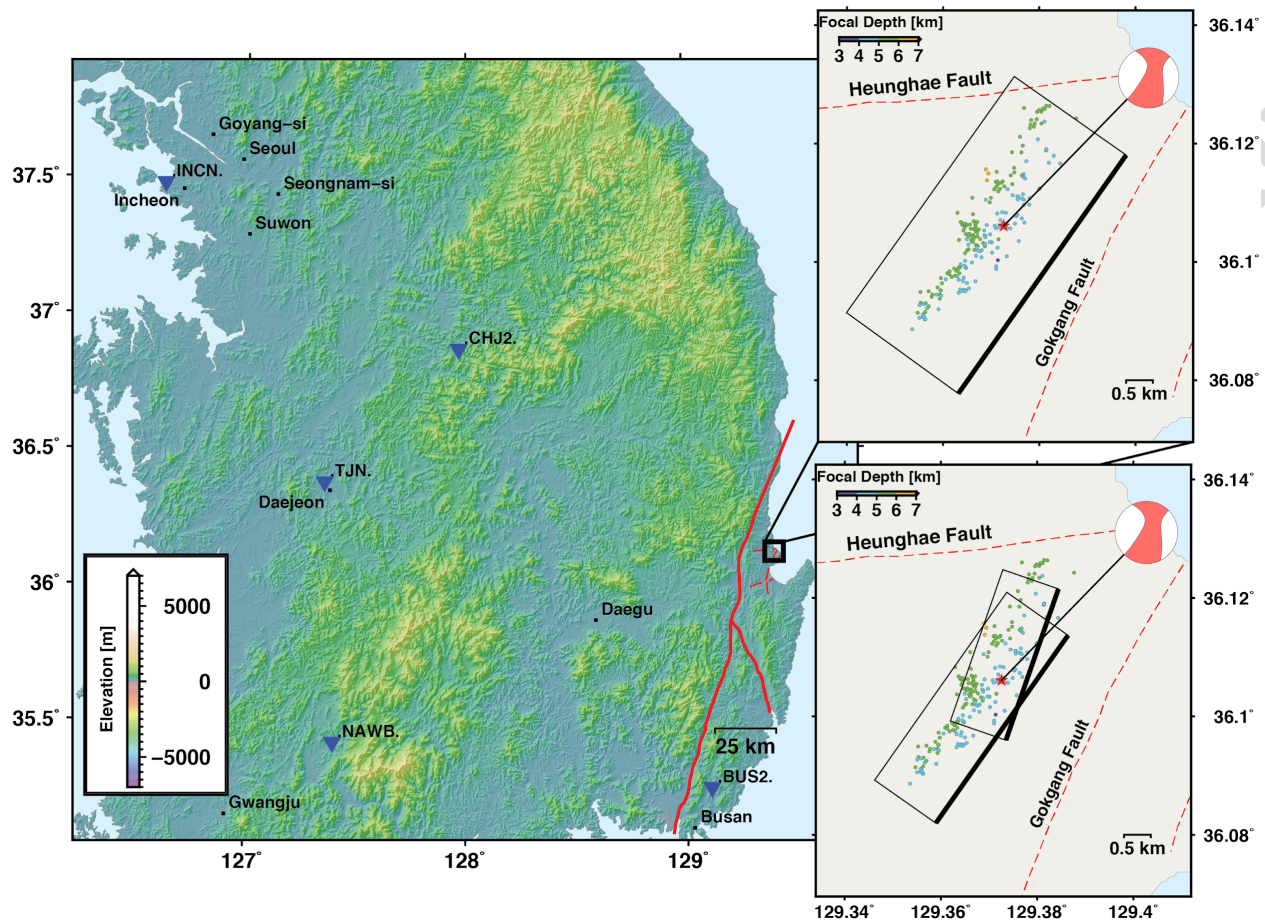
1130

1131   **Figure 1.** Map of the South Korean Peninsula showing the near-regional broadband stations (blue

1132   triangles). Solid and dashed lines represent the Yangsan and interpreted geological faults near the

1133   Pohang EGS site, respectively. The two inset plots present the location and geometry of the faults

1134   of Model 1F (upper panel) and Model 2F (lower panel). The thicker black lines mark the near-

1135   surface edge of the fault planes. Colored dots depict aftershocks locations extracted from Kim et

1136   al. (2018). The non-double-couple solution of Grigoli et al. (2018) is also shown.

1137

1138

Figure 2. Fault reconstruction using guided anisotropic location uncertainty distribution (g-ACLUD). a) Spatiotemporal density plot of the mainshock and aftershocks based on the nearest-neighbor distance. b), c) and d) Two fault plane geometry inferred by the g-ACLUD method. The main fault plane has a strike of 214° and dips at 65°, while the secondary fault plane has a strike 199° and dips at 60°. Black dots depict the seismicity used in this study. The geometry of the faults is shown in views b) as view from North, in c) as view from South, and d) in map view. The red star denotes the hypocenter of the Pohang earthquake.

1148

Figure 3. 3D rendering of the unstructured tetrahedral computational mesh, and the fault plane

with final slip on the 2-fault preferred model (Model 2F) of the Pohang earthquake (warm colors,

in m), and the radiated seismic wavefield 5 seconds after rupture initiation (cold colors, absolute

particle velocity in m/s). Note the strong effect of the high-resolution topography on modulating

the seismic wavefield.

1154

1155

1156

1157 **Figure 4**. Graphical summary of the outcome of 180 dynamic rupture simulations assuming

1158 different combinations of initial relative prestress ratio (R_0), fluid-pressure ratio (γ) and direction

1159 of S_{Hmax}. The corresponding 180 square frames are filled with color if the combination of

1160 parameters is able to trigger self-sustained rupture beyond the nucleation region on any fault. The

1161 S_{Hmax} direction is indicated by the size of the frame, leading to six imbricated frames for each set

1162 of prestress and fluid-pressure ratio parameters.

1163

1164
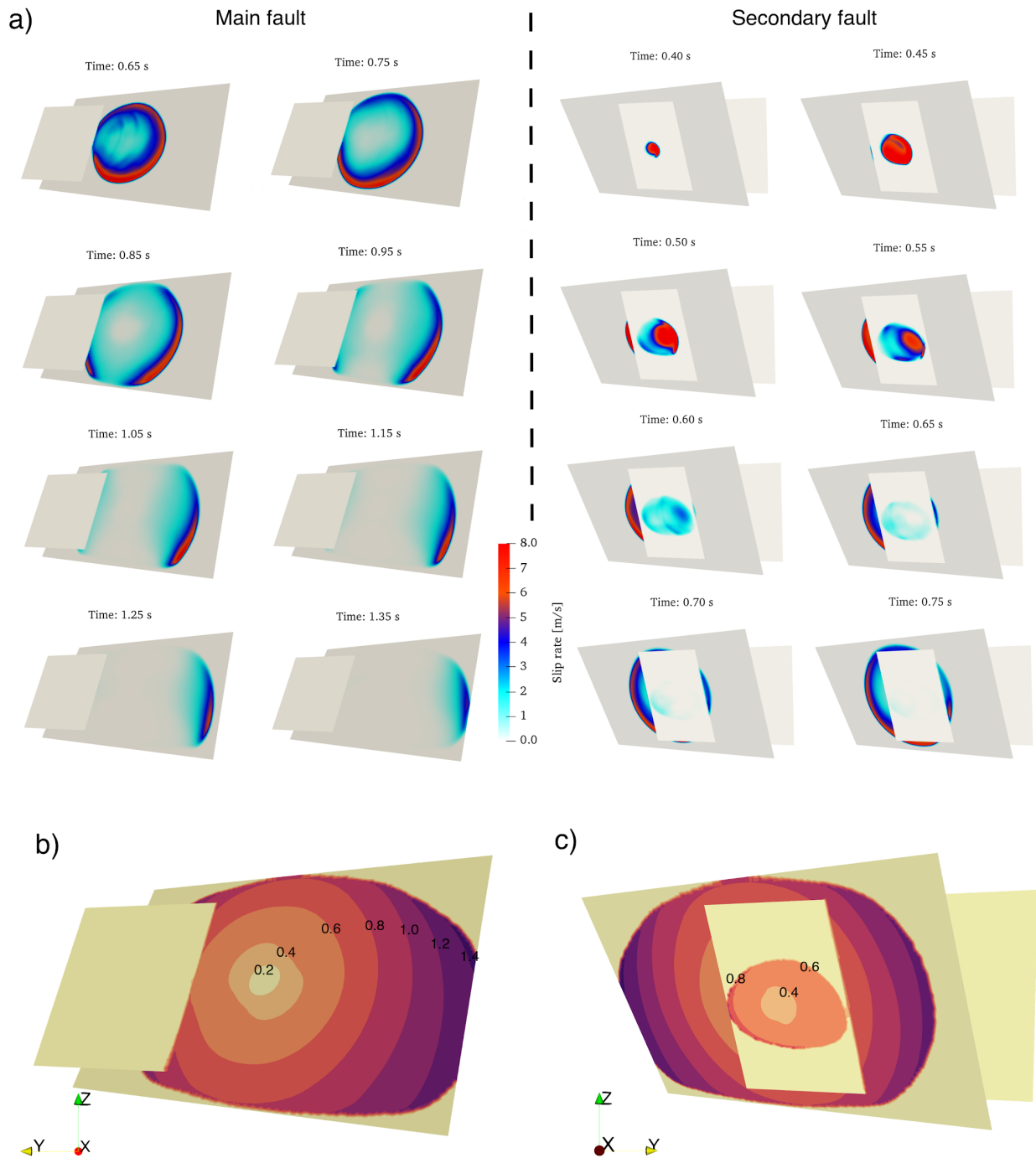
Figure 5. Overview of the simulated earthquake rupture of the preferred model (Model 2F), showing in a) and b) the space-time evolutions of the absolute slip-rate (in m/s) across the main

1165

1166

1167

1168

1169   and secondary fault plane. a) (left panel) view from North displaying the main fault rupture.

1170   Snapshots every 0.1 s. (right panel) view from South highlighting the rupture of a portion of the

1171   secondary fault. Snapshots every 0.05 s. b-c) Rupture-time contours at intervals of 0.2 s.

1172
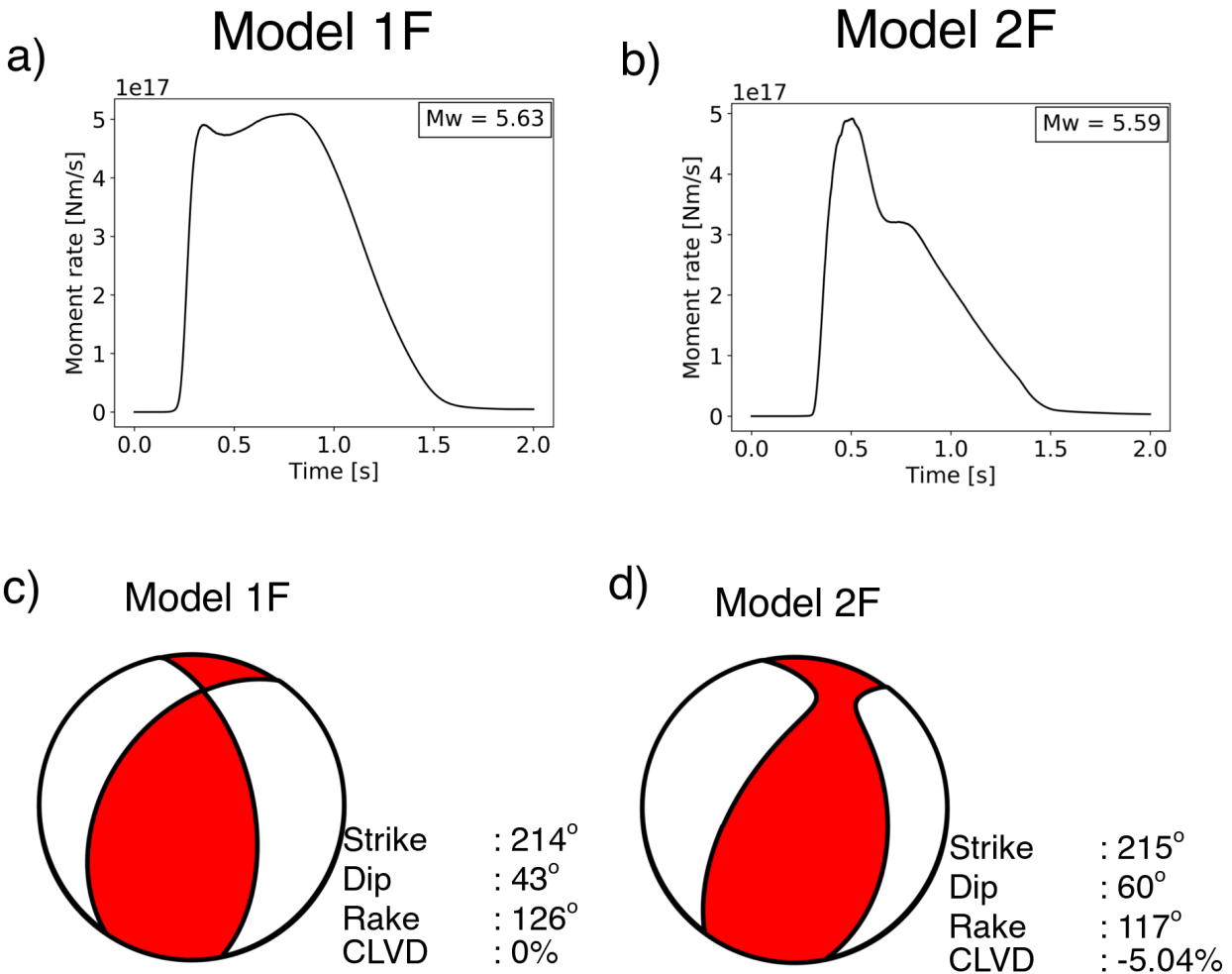
1173

1174   **Figure 6**. Moment rate release of a) Model 1F and b) Model 2F and moment tensor

1175   representation of the preferred one-fault c) and two-fault d) models.

1176
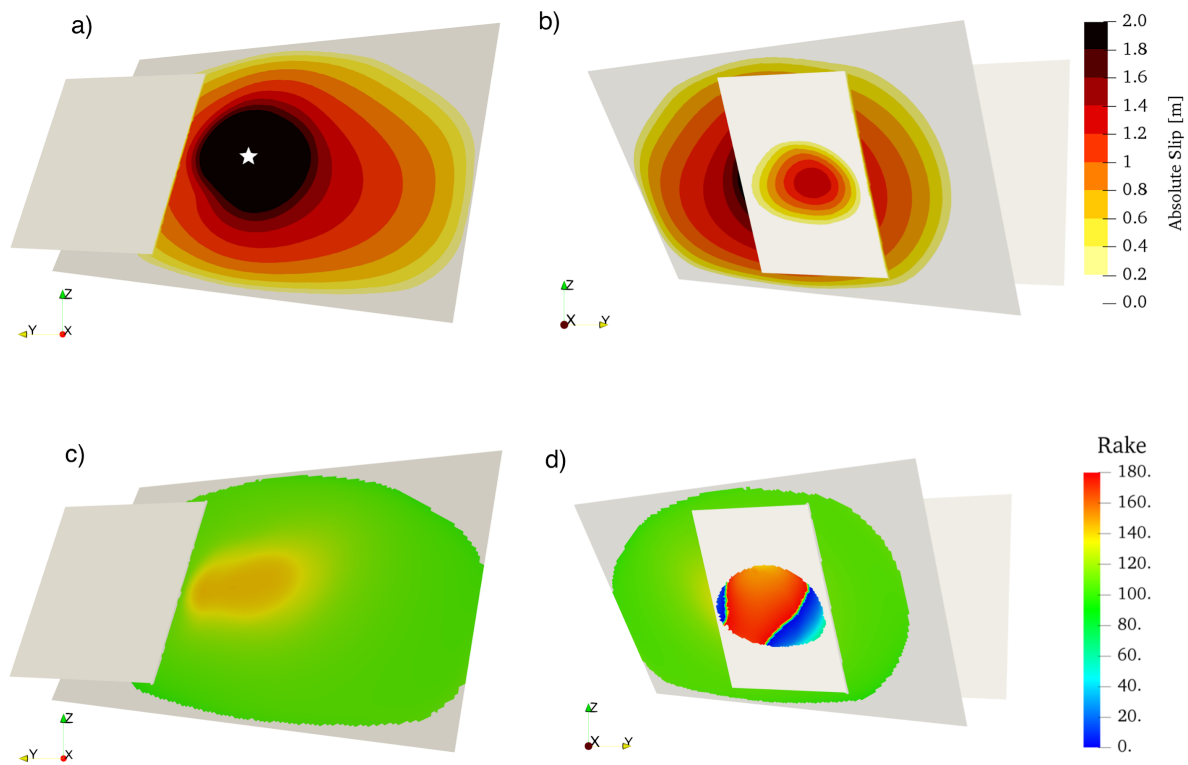
1177

Figure 7. Distribution of absolute fault slip (in m) in a) and b), and rake angles (in degrees) in c) and d) for the preferred dynamic rupture scenario (Model 2F) a) and c) view from North highlighting the main fault rupture. b) and d) view from South highlighting the rupture of a portion of the secondary fault. The white star in panel a) marks the considered hypocenter location.

1182

1183

1184

1185
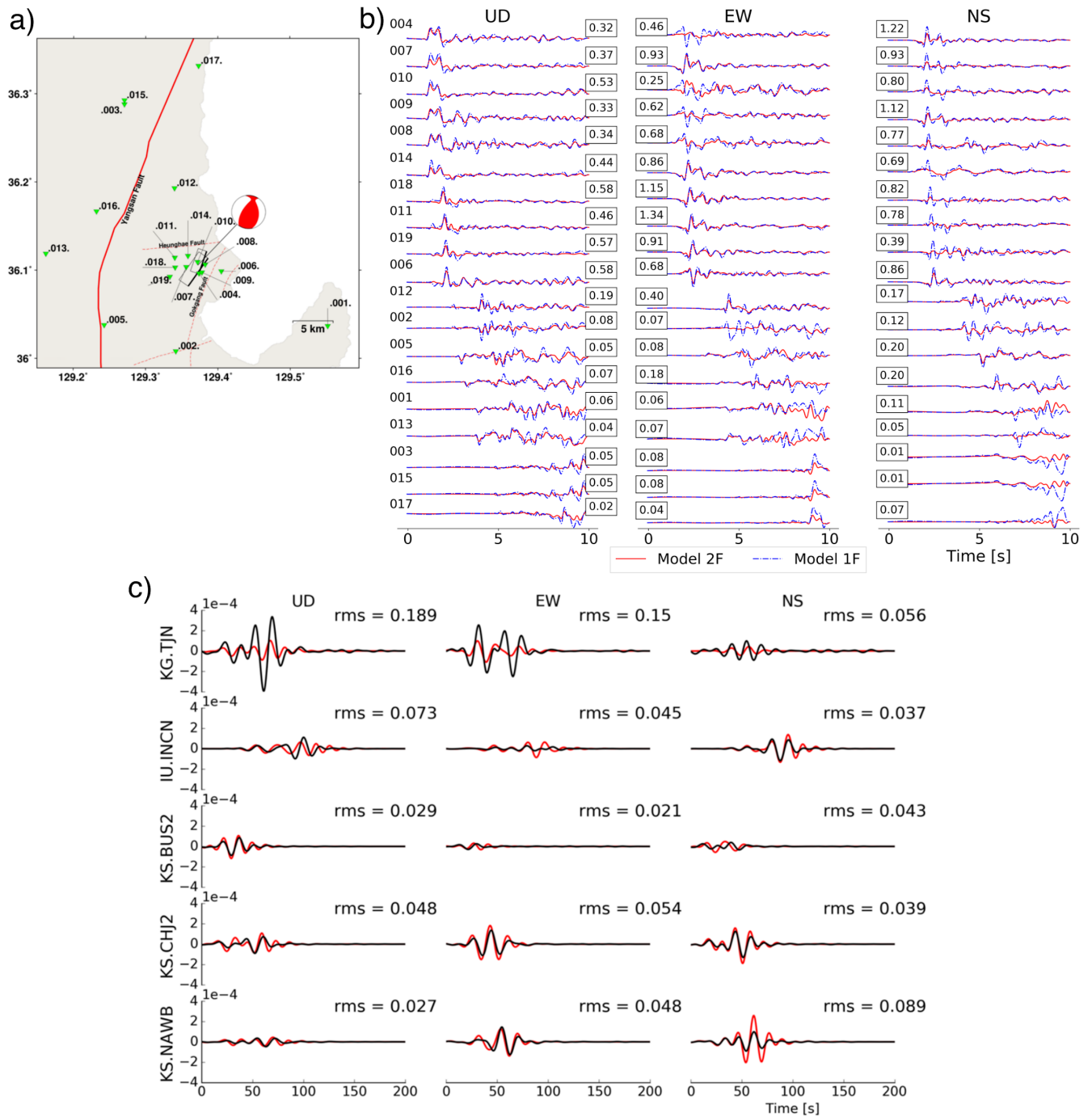
1186

1187 **Figure 8**. Comparison of synthetic and observed ground motion waveforms. a) Distribution of

1188 virtual stations (green triangles) at which synthetic waveforms are compared in b). The beachball

1189 is the moment tensor representation of the preferred 2 planes model scenario (Model 2F). Solid

1190 and dashed red lines represent the mapped Yangsan fault surface trace and the interpreted fault

1191   traces near the Pohang EGS site, respectively. The two rectangles show the location and geometry

1192   of the faults used in this study. b) Comparison of synthetic waveforms using one (Model 1F, blue

1193   dashed lines) and two fault planes (Model 2F, red solid lines) at the 19 dummy stations located in

1194   a). A 0.1 - 2 Hz 4th order Butterworth filter is applied to all traces. All traces are normalized. For

1195   each trace, the maximum velocity amplitude (in m/s) of Model 1F is indicated within a black

1196   square. c) Observed (black) and synthetic (red) waveforms for five regional stations for up-down

1197   (UD), east-west (EW) and north-south (NS) components (all located in South Korea, see blue

1198   triangles in Figure 1). t = 0 s denotes the origin time of the Pohang earthquake. A 0.033-0.08 Hz

1199 4th order Butterworth filter is applied to all traces. Synthetic regional waveforms are generated

1200   from the preferred dynamic rupture scenario Model 2F using Instaseis (Krischer et al., 2017) and

1201   2 s accurate Green's functions based on the PREM anisotropic model.

1202

1203

1204

1205
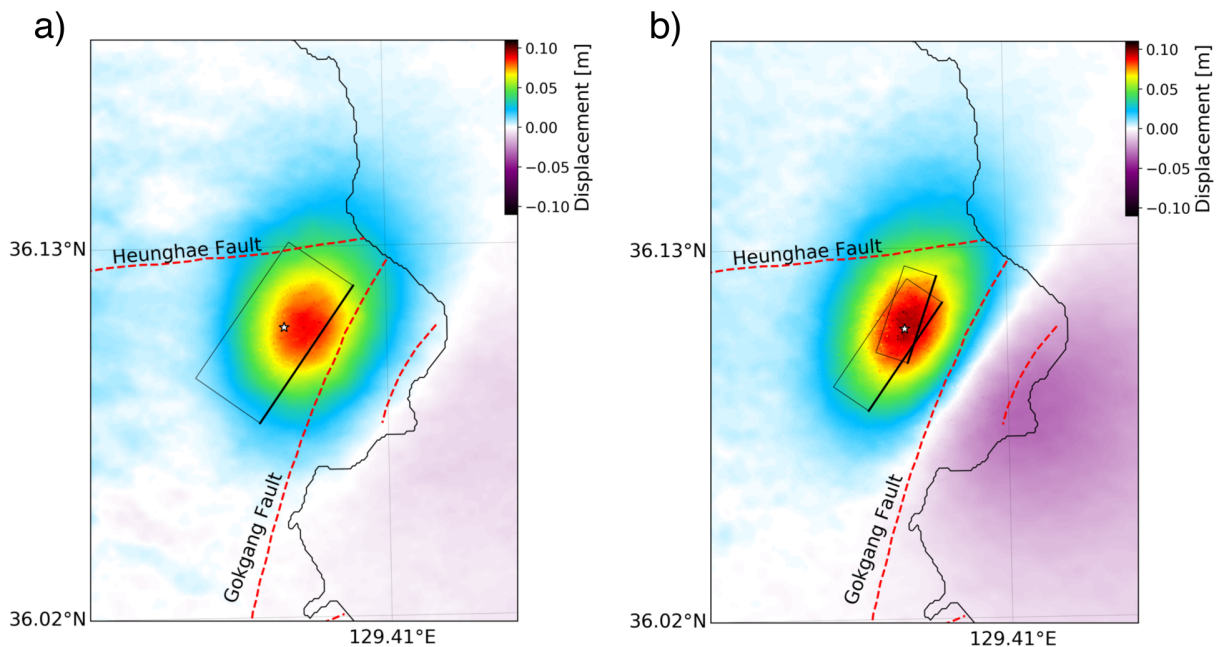
1206

1207 **Figure 9**. ((a) and (b)) Co-seismic surface displacements in the InSAR Line-of-sight (LoS)

1208 direction (in m) generated by a) Model 1F; one-plane (rectangle) and b) Model 2F; two-planes

1209 (two rectangles) preferred dynamic rupture scenario, respectively. The dashed red lines represent

1210 the traces of the interpreted faults near the EGS site.

1211

1212 **APPENDIX**

1213 **Friction parameters**

1214 To parameterize the frictional behavior, we use laboratory-based rapid velocity weakening friction

1215 law proposed by the community benchmark problem TPV104 Southern California Earthquake

1216 Center (SCEC-benchmark) (Harris et al., 2018). The friction law is adapted from - the formulation

1217 introduced by Dunham et al. (2011a). The governing equations in our notation are described in

1218 Ulrich et al. (2019a), the implementation in SeisSol (see **Data and Resources**) is described and

1219 verified in Pelties et al. (2014). Figure S1b shows the depth-dependent direct effect a and

1220   weakening slip velocity V_W. The evolution effect parameter b is set constant. We apply a velocity

1221   strengthening zone at the top 200 m of all faults to smoothly stop rupture. Within this zone, values

1222   for a and V_W increase linearly ranging from 0.01 and 0.1 m/s below depth of 3.3 km to 0.02 and

1223   1.0 m/s to the surface, respectively. Table A1 lists all friction parameters used in this study.

1224

1225   **Table A1**. Fault friction parameters assumed in this study

Parameter	Symbol	Value
Direct effect parameter	a	0.01 - 0.02 z≤3.3 km and 0.01 z > 3.3 km
Evolution effect parameter	b	0.014
Reference slip velocity	V_0	10^{-6} m/s
Steady-state friction coefficient at V_0	f_0	0.6
State-evolution distance	L	0.2 m
Weakening slip velocity	V_W	0.1 - 1.0 z≤3.3 km and 0.1 z > 3.3 km
Fully weakened friction coefficient	f_W	0.1
Initial slip rate	V_{ini}	10^{-16} m/s

1226

1227

1228

Nucleation procedure

1230   To nucleate the earthquake, we apply a time-dependent overstress centered at the hypocenter

1231   location, that is at longitude and latitude of 129.37° and 36.11°, respectively, and at a depth of 4.27

1232   km. The time-dependent overstressed nucleation area $R_{nuc}(t)$ is determined by increasing the

1233   initial relative prestress ratio R_0 as:

1234

1235 $$R_{nuc}(t) = R_0 + \Omega(r) \times S(t) \tag{A1}$$

1236

1237   where $\Omega(r)$ is a Gaussian-step function, r is the radius from the hypocenter, and $S(t)$ denotes the

1238   smoothed step function. The Gaussian-step function is defined as:

1239

1240 $$\Omega(r) = \xi \, exp(\frac{r^2}{r^2 - r_c{}^2}) \quad \text{for r} < r_c \; ; \qquad \Omega(r) = 0 \quad \text{otherwise} \tag{A2}$$

1241

1242   where ξ is the overstressed initial relative prestress ratio and $r_c = 500m$ is the radius of the

1243   nucleation patch. We only overstress the main fault plane; In the nucleation region, we set ξ to 2,

1244   and apply an overstress characterized by $S_{Hmax}= 77°$ and $v = 0.1$. These values are set by trial-

1245   and-error to allow rupture to propagate spontaneously with the least magnitude of overstress and

1246   to limit fault slip inside the nucleation patch. The orientation of S_{Hmax} is also in accordance with

1247   Korean Government Commission, 2019 and Ellsworth et al. (2019) which suggest optimally

1248   oriented stress orientation and critically stressed inside the nucleation zone. The smoothed step

1249   function is formulated as:

1250

1251 $$S(t) = exp\left(\frac{(t-T)^2}{t\times(t-2\times T)}\right) \quad \text{for } 0 < t < T; S(t) = 1 \quad \text{for } t \geq T \qquad \text{(A3)}$$

1252

1253 where $T = 0.4$ s is the nucleation time.

1254

1255 Numerical method

1256 We use the open-source software SeisSol (Dumbser and Käser, 2006; Pelties et al., 2014; Uphoff

1257 et al., 2017; Wollherr et al., 2018) (see **Data and Resources**), which couples seismic wave

1258 propagation in complex media and frictional fault failure. SeisSol uses an Arbitrary high-order

1259 DERivative-Discontinuous Galerkin (ADER-DG) approach which achieves high-order accuracy

1260 in space and time (Käser and Dumbser, 2006). SeisSol uses flexible non-uniform unstructured

1261 tetrahedral mesh, which allows accounting for complex geometric features such as 3D fault

1262 networks or high-resolution topography across a large range of scales: from small-scale fault

1263 roughness, large-scale fault structures to fault-to-fault interaction. Dynamic rupture simulations

1264 are sensitive to geometrically complexity of faults (Dunham et al., 2011b; Shi and Day, 2013;

1265 Uphoff et al., 2017; Wollherr et al., 2018, 2019; Ulrich et al., 2019a, 2019b).

1266   A high resolution and accurate simulation are essential to resolve the detailed processes of

1267 rupture propagation of the intersected fault geometry. We motivate the presented deterministic

1268 parameter study with the computational feasibility of many such simulations. While the feasibility

1269 of dynamic rupture inversion and statistical learning approaches has been demonstrated (e.g.

1270 Peyrat et al. 2001; Bauer et al., 2018, Happ et al. 2019, Gallovič et al. 2019a, Gallovič et al. 2019b),

1271 these are restricted by near-field data availability and the computational cost of each forward

1272 dynamic rupture model.

1273 SeisSol is verified in a wide range of benchmark problems, including dipping faults,

1274 branched and curved faults, on-fault heterogeneity, and laboratory-based friction laws (de la

1275 Puente et al., 2009; Pelties et al., 2012; Pelties et al., 2014; Wollherr et al., 2018,) in line with the

1276 SCEC-Benchmark Dynamic Rupture code verification exercises (Harris et al., 2011; Harris et al.,

1277 2018) as well as against analytical reference solutions for seismic wave propagation (e.g., Uphoff

1278 and Bader, 2016; Wolf et al., 2020). Fast time to solution is achieved using end-to-end optimization

1279 (Breuer et al., 2014; Heinecke et al., 2014; Rettenberger et al., 2016), including an efficient local

1280 time-stepping algorithm (Breuer et al., 2016, Uphoff et al., 2017). This efficient algorithm on high-

1281 performance computing architecture provides up to ten-fold speed up (Uphoff et al., 2017).

1282 SeisSol allows accounting for off-fault yielding. Inelastic energy dissipation influences

1283 rupture dynamics such as rupture speed and rupture style (e.g., Gabriel et al., 2013). Off-fault

1284 plasticity is incorporated using the off-line code generator to compute matrix operations in an

1285 efficient way (Wollherr et al., 2018). SeisSol also supports visco-elastic rheologies, using an off-

1286 line code generator similar to that off-fault plasticity. In this study, we use a spatiotemporal

1287 discretization of polynomial degree $p = 4$ ($O5$) for all simulations.

1288

1289 **Mesh generation**

1290 The simulation domain and fault plane geometry model are created using third-party software

1291 GoCad (Emerson paradigm holding, 2018) in a Cartesian coordinate system. We discretize the

1292 unstructured tetrahedral mesh using the meshing software Simmodeler (Simmetrix Inc., 2017).

1293 The mesh element edge length size to 50 m close to the fault plane and 200 m at the surface

1294   topography, yielding a 4 million volume cell mesh. The mesh size on the fault plane is examined

1295   prior to the simulation by calculating the cohesive zone (or process zone) to ensure convergence.

1296   Wollherr et al. (2018, 2019) provide a way to resolve the cohesive zone for the case of SeisSol. To

1297   save the computational costs and at the same time avoid reflection from the domain boundary, we

1298   gradually increase the edge length size of the tetrahedral element by a factor of 6% away from the

1299   fault plane and surface topography. Figure 3 depicts the unstructured tetrahedral mesh used in this

1300   study, overlain by a snapshot of the absolute velocity field at simulation time 5 s, for our preferred

1301   dynamic rupture model (Model 2F), highlighting the effect of the topography on the near-field

1302   ground motions.

1303   The locally refined mesh and high-order spatiotemporal discretization allow capturing the

1304   high-frequency content of the waveforms with high accuracy (little numerical dispersion),

1305   especially in the near-fault region. We estimate the maximum resolved frequency is up to 4 Hz

1306   within 7 km distance from the fault zone, and around 1 Hz at 30 km distance from the fault.

1307   Simulating 5 s typically requires 15 minutes (average run-time) on Intel Haswell cores with 128

1308   nodes using supercomputer Cray XC40 Shaheen-II, King Abdullah University of Science and

1309   Technology, Saudi Arabia.

1310

1311   **Supplemental Material for**

1312   # Dynamic fault interaction during a fluid-injection induced

1313   # earthquake: The 2017 Mw 5.5 Pohang event

1314   **K. H. Palgunadi, A.-A Gabriel, T. Ulrich, J. A. Lopéz-Comino, P. M. Mai**

1315

1316   This supplement includes additional figures, a table, a zipped file and videos supporting

1317   the outcome of the study. The figures consist of depth-dependent 1D subsurface material and

1318   friction parameters, part of static modeling, peak slip-rate distribution, off-fault plastic

1319   deformation, synthetic surface displacements, and shake-map. The table contains the rake of initial

1320   traction of two-fault planes geometry using static modeling. The zipped file consists of all

1321   parameters used for the preferred two-fault planes scenario. The videos show snapshots of the slip-

1322   rate in two perspective views (presenting the main and secondary fault plane) of the preferred two-

1323   fault planes scenario.

1324

1325   **LIST OF SUPPLEMENTAL TABLE CAPTIONS:**

1326   **Table S1.** Rake of initial shear traction on the faults of Model 2F

1327

1328   **LIST OF SUPPLEMENTAL FIGURE CAPTIONS:**

1329   **Figure S1**. Vertical profiles of a) the 1-D model of seismic wave speeds by Woo et al. (2019) and

1330   by Korean Government Commission (2019). Panel b) displays the depth-dependent parameters of

1331   the velocity weakening rate-and-state friction law.

1332

1333 **Figure S2**. Rake of initial (at t=0) shear traction for exemplary orientations of maximum horizontal

1334 stress S_{Hmax} (see also Table S1). Thrust-faulting is favoured for S_{Hmax}=120°. Note that

1335 S_{Hmax}=77° corresponds to the findings of Ellsworth et al. (2019).

1336

1337 **Figure S3**. Peak slip-rate of the Model 2F. The maximum peak slip rate (saturated yellow color)

1338 outside the nucleation zone is 15 m/s. View from a) North and b) South.

1339

1340 **Figure S4.** Asymmetric off-fault plastic deformation for Model 1F (a and b) and for Model 2F (c

1341 and d). a) and c) view from North b) and d) view from South. The accumulated volumetric plastic

1342 strain is mapped into the scalar quantity η as noted by the purple colorbar.

1343

1344 **Figure S5.** Surface displacements. a) Co-seismic surface displacements using only the main fault

1345 plane of Model 2F. Rectangle illustrates the fault plane. b) Residual of Model 2F with respect to

1346 Model 2F by using only the main fault plane. The dashed red lines represent the traces of the

1347 interpreted faults near the EGS site. The white star represents the epicenter of the Pohang

1348 earthquake.

1349

1350 **Figure S6.** Peak ground velocity shake-map (in m/s, based on GMRotD50 (Boore et al., 2006))

1351 for preferred scenario Model 2F, color-contoured 0.2 increments. The white star denotes the

1352 epicenter of the Pohang earthquake.

1353

1354

1355

1356   **LIST OF SUPPLEMENTAL FILES:**

1357   **Video S1**. Slip-rate of Model 2F. The video also can be accessed in

1358   https://drive.google.com/open?id=1nm3HZ_YOD-j8t_YatTFfs9prVKplEExj

1359   **Parameters.zip** (this file contains all parameters used for the preferred Model 2F)

1360

1361 **LIST OF SUPPLEMENTAL TABLES:**

1362 **Table S1.** Rake of initial shear traction on the faults of Model 2F

S_{Hmax}	Main fault rake (°)	Secondary fault rake (°)
52	0	12
57	3	16
62	7	20
67	11	24
72	15	29
77	19	35
82	23	41
87	28	48
92	34	57
97	40	66
102	47	77
107	55	88
112	64	100
120	80	110
125	91	130
130	110	140
135	115	130
140	120	150

1363

1364   **LIST OF SUPPLEMENTAL FIGURES:**
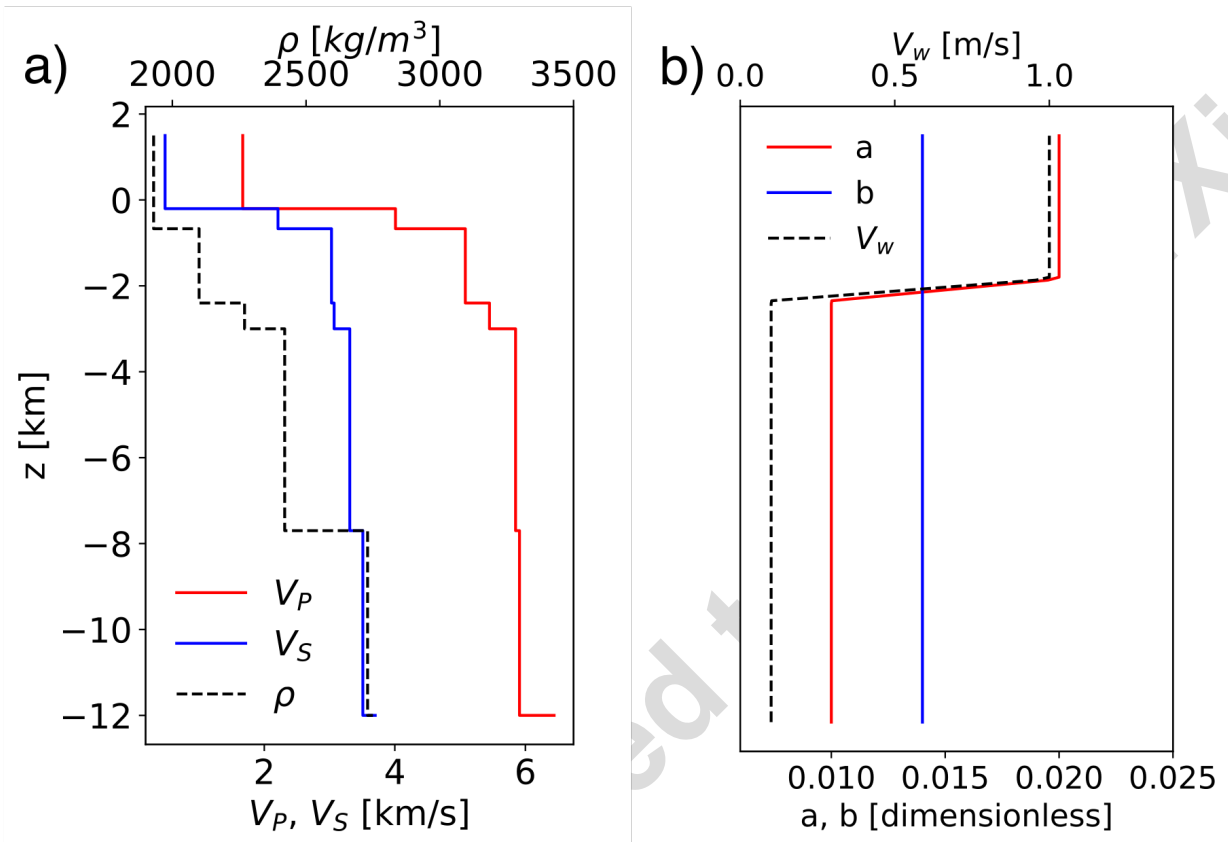
1365

1366   **Figure S1**. Vertical profiles of a) the 1-D model of seismic wave speeds by Woo et al. (2019) and

1367   by Korean Government Commission (2019). Panel b) displays the depth-dependent parameters of

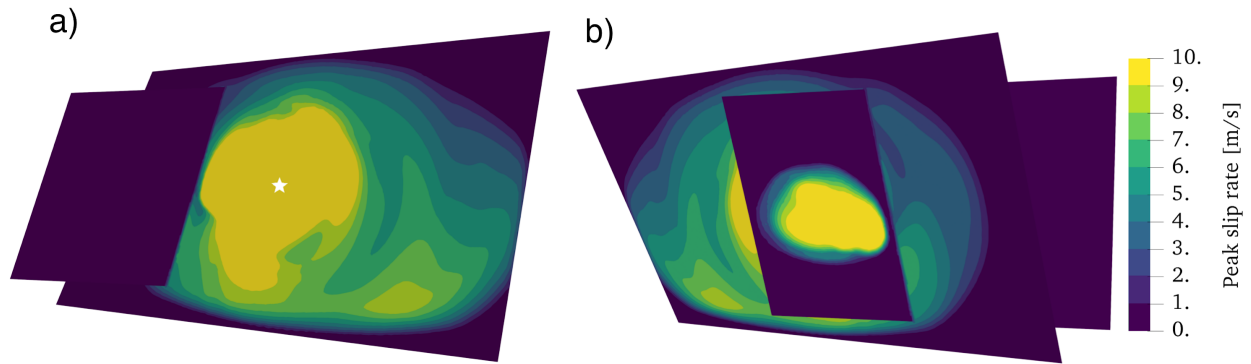1368   the velocity weakening rate-and-state friction law.

1369
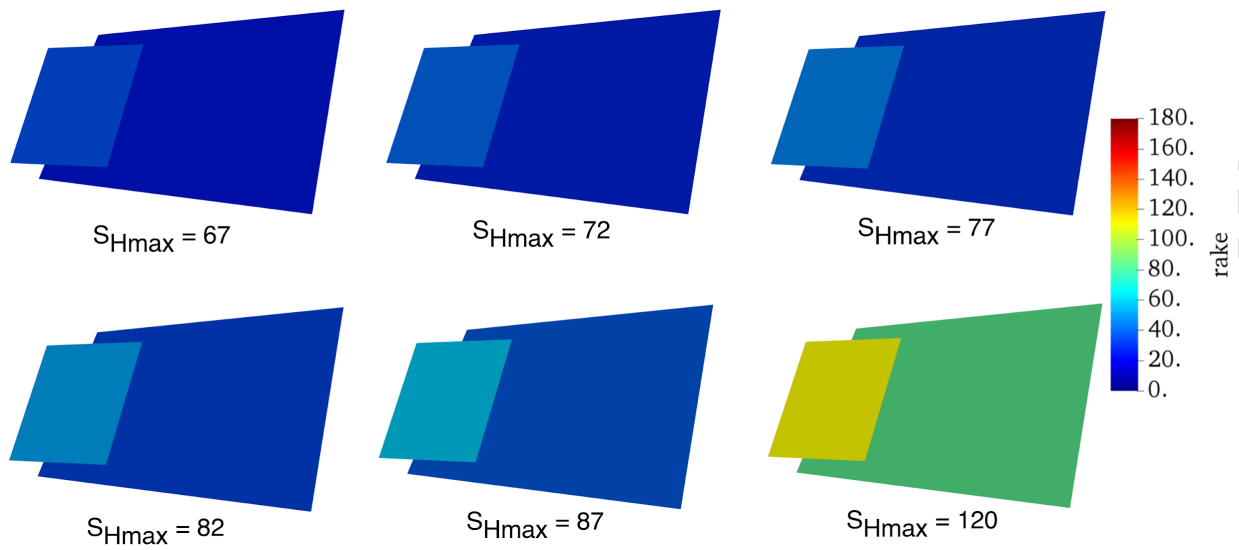
1370

Figure S2. Rake of initial (at t=0) shear traction for exemplary orientations of maximum horizontal

stress S_{Hmax} (see also Table S1). Thrust-faulting is favoured for S_{Hmax}=120°. Note that

S_{Hmax}=77° corresponds to the findings of Ellsworth et al. (2019).
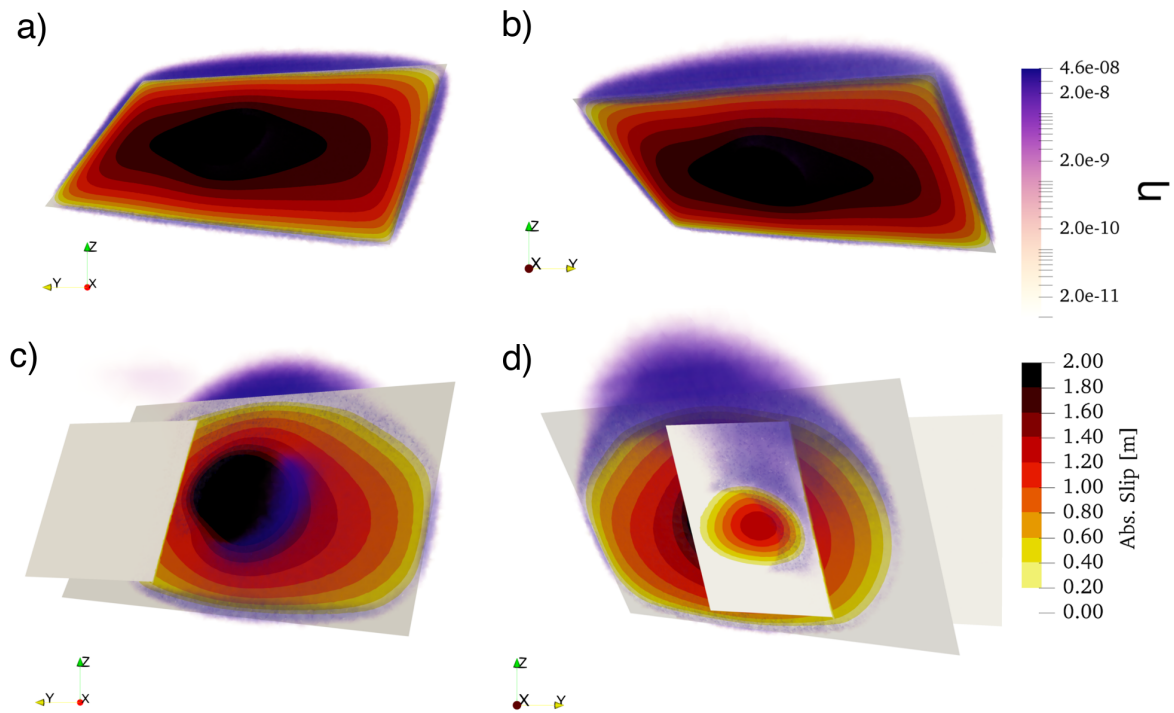
1371

1372

1373

1374

1375

a)   b)

1376

1377   **Figure S3**. Peak slip-rate of the Model 2F. The maximum peak slip rate (saturated yellow color)

1378   outside the nucleation zone is 15 m/s. View from a) North and b) South.
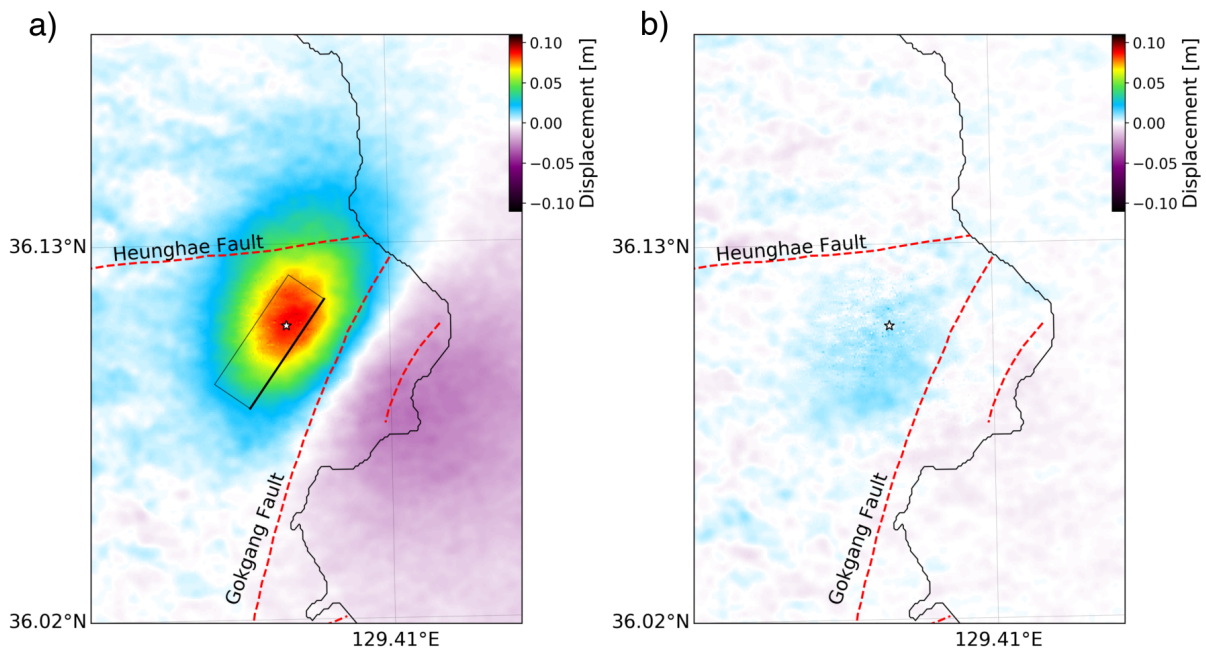
1379

Figure S4. Asymmetric off-fault plastic deformation for Model 1F (a and b) and for Model 2F (c and d). a) and c) view from North b) and d) view from South. The accumulated volumetric plastic strain is mapped into the scalar quantity η as noted by the purple colorbar.

1385

1386   **Figure S5.** Surface displacements. a) Co-seismic surface displacements using only the main fault

1387   plane of Model 2F. Rectangle illustrates the fault plane. b) Residual of Model 2F with respect to

1388   Model 2F by using only the main fault plane. The dashed red lines represent the traces of the

1389   interpreted faults near the EGS site. The white star represents the epicenter of the Pohang

1390   earthquake.

1391
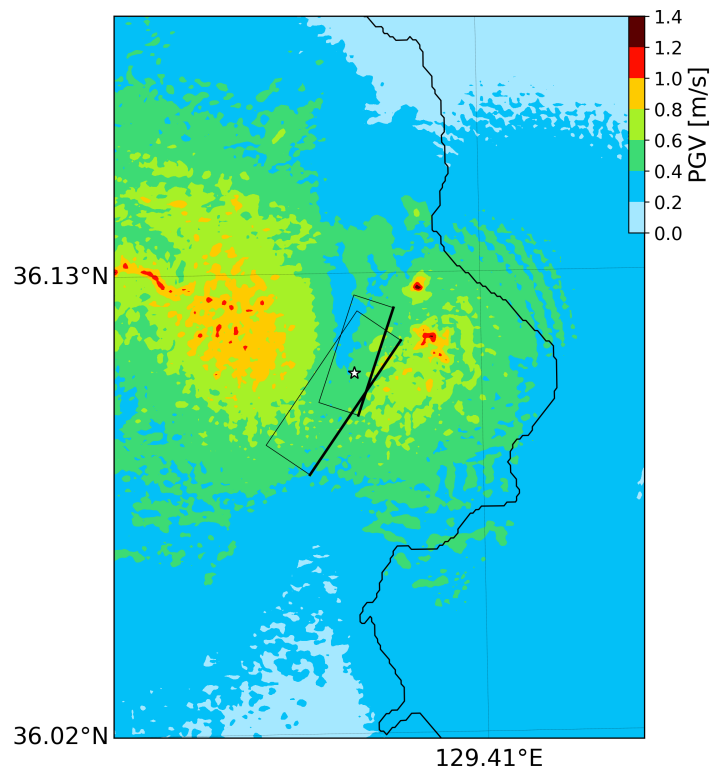
1392

1393   **Figure S6.** Peak ground velocity shake-map (in m/s, based on GMRotD50 (Boore et al., 2006))

1394   for preferred scenario Model 2F, color-contoured 0.2 increments. The white star denotes the

1395   epicenter of the Pohang earthquake.

1396

1397

1398

1399

1400

References:

1402   Boore, D. M., J. Watson-Lamprey, and N. A. Abrahamson, 2006, Orientation-Independent

1403   Measures of Ground Motion, Bull. Seismol. Soc. Am., 96, no. 4A, 1502–1511, doi:

1404   10.1785/0120050209.

1405   Ellsworth, W. L., D. Giardini, J. Townend, S. Ge, and T. Shimamoto, 2019, Triggering of the

1406   Pohang, Korea, Earthquake (Mw 5.5) by enhanced geothermal system stimulation,

1407   Seismological Society of America, 1844–1858.

1408   Korean Government Commission, 2019, Summary Report of the Korean Government

1409   Commission on Relations between the 2017 Pohang Earthquake and EGS Project.

1410   Woo, J. -U., M. Kim, D. -H. Sheen, T. -S. Kang, J. Rhie, F. Grigoli, W. L. Ellsworth, and D.

1411   Giardini, 2019, An In-Depth Seismological Analysis Revealing a Causal Link Between the

1412   2017 M $_W$ 5.5 Pohang Earthquake and EGS Project, J. Geophys. Res. Solid Earth,

1413   2019JB018368, doi: 10.1029/2019JB018368.

1414

1415

1416
1417